Discovery of frequency-sweeping millisecond solar radio bursts near 1400 MHz with a small interferometer

Eric R. Evarts

Brandeis University

Abstract

While testing the Small Radio Telescope Interferometer at Haystack Observatory, we noticed occasional strong fringes on the Sun. Upon closer study of this activity, I find that each significant burst corresponds to an X-ray solar flare and corresponds to data observed by RSTN. At very short integrations (512 μs), most bursts disappear in the noise, but a few still show very strong fringes. Studying these <25 events at 512 μs integration reveals 2 types of burst: one with frequency structure and one without. Bursts with frequency structure have a brightness temperature ~10^{13}K, while bursts without frequency structure have a brightness temperature ~10^{8}K. These bursts are studied at higher frequency resolution than any previous solar study revealing a very distinct structure that is not currently understood.

Table of Contents

Introduction

During the summer of 2005, we set up and tested a new Small Radio Telescope Interferometer at Haystack Observatory in Westford, MA. When testing this interferometer, we observed Cygnus A and the Sun. Our initial belief was that we should be able to resolve the two lobes of Cygnus A and that we should be able to identify a sunspot on the Sun. We succeeded in resolving the two lobes of Cygnus A, but when we observed the Sun, we were met with a few surprises. While we never succeeded in identifying a sunspot, we did observe various kinds of bursting activity on the Sun in the 1400 MHz frequency band. After a little digging, we found very little information about any type of Solar activity around 1400 MHz, and so we set out to learn more about these bursts.

The primary goal of this project is to better understand this burst activity on the Sun. More specifically, we attempt to show some connection between the radio bursts we are observing and solar flares observed by the GOES Satellites. Upon a closer look, we have examined the Sun at higher frequency resolution than anyone who has previously studied the Sun.

Interferometry Crash Course

Most people have looked through an optical telescope at some time in their lives. With a small amount of effort and a reasonable explanation, one can understand how this optical device works by converging the light though a set of lens to produce a focused image. In a broad sense, radio telescopes work the same way: radio waves of a particular wavelength are collected and focused onto a radio receiver feed. Interferometry allows radio astronomers to use multiple radio telescopes to "pretend" that they are using a single larger telescope.

By using multiple antennas, the data recorded can be Fourier Transformed to create an image with much higher resolution than using any one of the single antennas. Using a two element interferometer, we can learn more information about the distant object than with a single dish, but an image cannot be created with the single Fourier component observed with one baseline.

To better understand how a radio interferometer works, there are several experiments that are very well known that use the concept of an interference pattern. First, consider the double slit experiment: shine monochromatic light onto a screen that only allows the light to pass through two parallel slits, then observe the pattern projected on a screen some distance away. With only one slit open, a spot the shape of the beam is seen on the screen. With two slits, a pattern of the interference is seen, which means that there is a central maximum where complete constructive interference reinforces the signal surrounded by minimums at the points where complete destructive interference eliminated the signal. Each successive maximum away from the center is weaker until no signal can any longer be detected. Each successive maximum is a distance away from the previous maximum that is proportional to the number of complete wavelengths between the maximums. The width of the primary maximum in the middle is dependent upon the


Figure 1 Double slit experiment observed results with both slits open. Each peak is an integer multiple of wavelengths (times a constant based on the details of the setup) away from the center of the pattern. Image courtesy of Wikipedia.
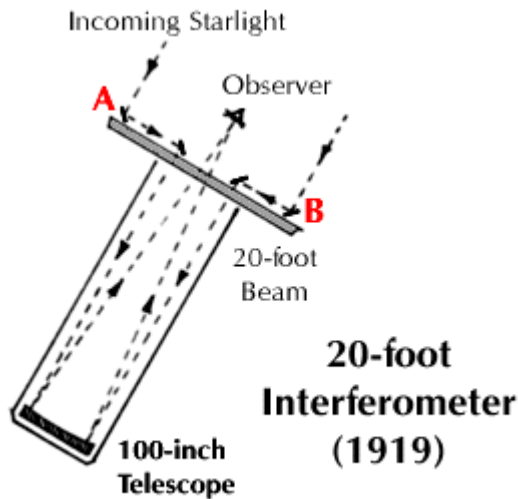
Figure 2 The Michelson interferometer. This extension of the double slit experiment to astronomical measurements proved able to use the interference pattern to measure the diameters of the Galilean moons of Jupiter. This same principle applied to radio waves instead of visible light is the foundation of a radio telescope interferometer. Image courtesy of Sydney University Stellar Interferometer website.

wavelength of the light. The distance between the maximums, called the fringe spacing, is also dependent upon the distance between the slits and the distance to the screen.

The next experiment of interest is the Michelson Stellar Interferometer. This experiment extended the concept of the double-slit experiment and applied it to astronomy. By attaching two mirrors to the Mount Wilson 100 inch telescope, Michelson observed an interference pattern that allowed him to determine the diameter of the Galilean moons of Jupiter. This same principle is used for radio interferometery, but certain electronics replace the converging mirror of the Mount Wilson telescope.

The speed of modern electronics allows all of the applicable information about a radio wave to be recorded to some medium, be it tape or disk. By performing various calculations to data obtained using multiple elements, radio astronomers can reconstruct an image that has the same resolution as if it was recorded with a telescope with a diameter of the projected distance between the two telescopes used to make the recordings.

The simplest interferometer is a connected element interferometer. In a connected element interferometer, the signal from each antenna is mixed with the output of a single local oscillator to adjust the signal into a frequency that is easier to work with in the electronics. This mixed signal is then amplified and filtered to allow for proper processing. There is a known delay between when the signal arrives at the first element and when the signal arrives at the second element. By delaying the first signal by the time it takes for the signal to arrive at the second element, and then multiplying the signals together, the output of the combined signals is obtained.

To create a larger interferometer requires either longer cables or a way to not require the elements to be connected. Longer cables can only work up to a certain point because of signal loss due to cable transmission. To remove the connection will require two oscillators instead of just one local oscillator. The biggest difficulty in using two oscillators is the accuracy from oscillator to oscillator. The advent of very precise atomic clocks allows one to be confident that the period of each oscillator is close enough to be treated as the same. By mixing the signal with the output from an atomic clock allows the single local oscillator to be replaced with two different atomic clocks. The other challenge with removing the connection between elements requires

6
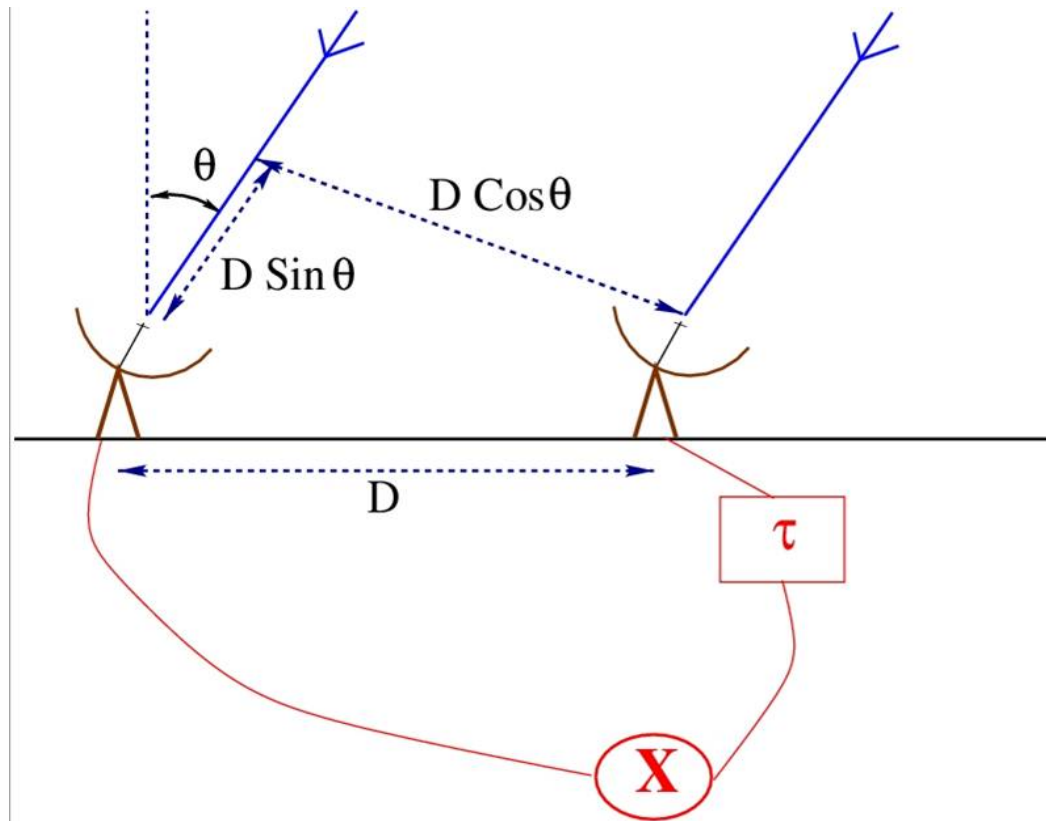
Figure 3 A Two Element Connected Interferometer. In connected interferometry, the elements are both connected to a multiplier (X), with one signal delayed by delay τ. Additionally, both elements are connected to a single local oscillator that is used to reduce the frequency of the signal to a frequency that is easier to handle in the electronics and easier to transmit along cables to the multiplier. In order for the same part of a plane wave from one element to be aligned with the signal at the second element, a delay, τ, must be inserted into the first signal in order to allow that same signal to reach the second element. In this figure, the delay must be equal to D Sin θ. The projected distance between the elements as seen by the object being observed is equal to D Cos θ.

storing the data in some fashion that allows the final combining of the data to be done at some different time. In order to keep track of the correct recordings, a timestamp must also be attached to the data in addition to mixing down with a local oscillator. This timestamp is used to ensure that the correct parts of the data are multiplied together, after applying the correct delay time as in the connected element case.

For interferometry to work, each telescope must very accurately record the time of each sample. These timestamps and other information, such as the precise positions of each telescope involved, are vital to our ability to reconstruct the data into a meaningful format. For any point in the sky, one can calculate when a plane wave will arrive at each antenna in the interferometer. By aligning the data so that the information from one plane wave at one antenna is matched with the information about that same plane wave at the other antenna, we achieve the same result as if we used an antenna the size of the distance between the two antennas as it appears to the object we are observing (instead of the actual distance, we use the projected distance). Once one knows the right parts of the data stream to put together, certain calculations allow computation of fringe amplitude and other information about the signals being observed. The fringe amplitude is comparable to the flux measured by a single dish recording. In radio astronomy, the equipment is fast enough to record the phase of the signal in addition to the flux, so as a primary diagnostic to determine the presence of a

signal one examines the phase signature of the correlated data. If the phase varies smoothly across an event, it is very likely that a significant signal exists. At all other times, when a coherent signal does not exist, the phase of adjacent photons will be arbitrary and therefore the phase will not vary smoothly. As an additional diagnostic to determine if a true signal is being observed, part of the computation involves looking at a range of delays around the geometrically computed delay. If a signal really exists where the interferometer is looking, the largest fringe amplitude will be seen very close to the geometrically computed delay. If a signal is not in the data, or if the signal is not where the interferometer is looking, the maximum fringe amplitude will be seen at some other delay.

The Small Radio Telescope Interferometer

All of our data were recorded using the Small Radio Telescope Interferometer at Haystack Observatory in Westford, MA. Data came from two antennas, one at Haystack, the second at Westford Telescope, using a baseline of 1.4 km.

Figure 4 A Small Radio Telescope in Action at the Westford site.

Hardware

These second generation Small Radio Telescopes use a 2.1 m standard television satellite receiver dish attached to proprietary receiver hardware. The feed on the antenna is designed to receive circularly polarized radio signals in the range 1300 MHz to 1700 MHz with peak performance around 1400 MHz. A preamp attached to the feed boosts the signal strength to transmit the signal to the receiver hardware in a nearby building or other enclosure.

The receiver box consists of a consumer computer system running Gentoo Linux (Kernel 2.4 or 2.6) connected to other recording hardware. This particular generation of the hardware is the first to use GPS timing and location units in each receiver allowing for VLBI-type interferometry with independent (unconnected) systems. This box houses the motor control unit and proprietary receiver and signal processing hardware. The receiver and processing hardware connects to the internal computer through USB 2.0, a necessity due to the high throughput demands required to transfer all of the data. The remaining control hardware connects to the master computer through RS-232 serial connections.

We use the systems in VLBI Mode. In this mode each system records data and attaches a very accurate timestamp from the GPS timing unit. To keep the data stream at a manageable volume, the system records 1 bit per sample with a sampling rate of 8 Mega-samples per second. This 1 bit data can be restored to the original signal curve using Van Vleck correction. The data are stored on the Small Radio Telescope's hard drive until software correlation is later performed using a stand-alone system. Due to the system design, data are recorded for 8/10 of a second, then the remaining 2/10 of the second is used to write the data to the hard drive. While the system is recording, the software suspends all other activities on the computer, so there must be pauses in the recording in order for the computer system to not crash. As such, we recorded data using a 1 minute on, 1 minute off pattern while

Figure 5 The inner workings of the SRT receiver box: Linux PC (red, left), GPS Receiver (green, center), signal processing controller (green, top right), motor controller (green, center right)

the sun was in the sky.

While observing with the interferometer, we discovered that there are certain unexpected limitation of the hardware that need to be addressed. The most relevant limitation we found is the stability of the GPS unit. When trying to integrate for much longer than approximately half of a second, we discovered fringe amplitudes dropped significantly. After closer study we determined that the GPS unit timing signals can vary up to a couple of nanoseconds from small temperature variations near the unit. This temperature variation causes fringe rotation that originally went uncorrected in the software correlator. By adding a first order fringe rotation term to the software correlator, we have improved the coherence time from 0.5 seconds to approximately 7 seconds, something important for most radio astronomical observations.
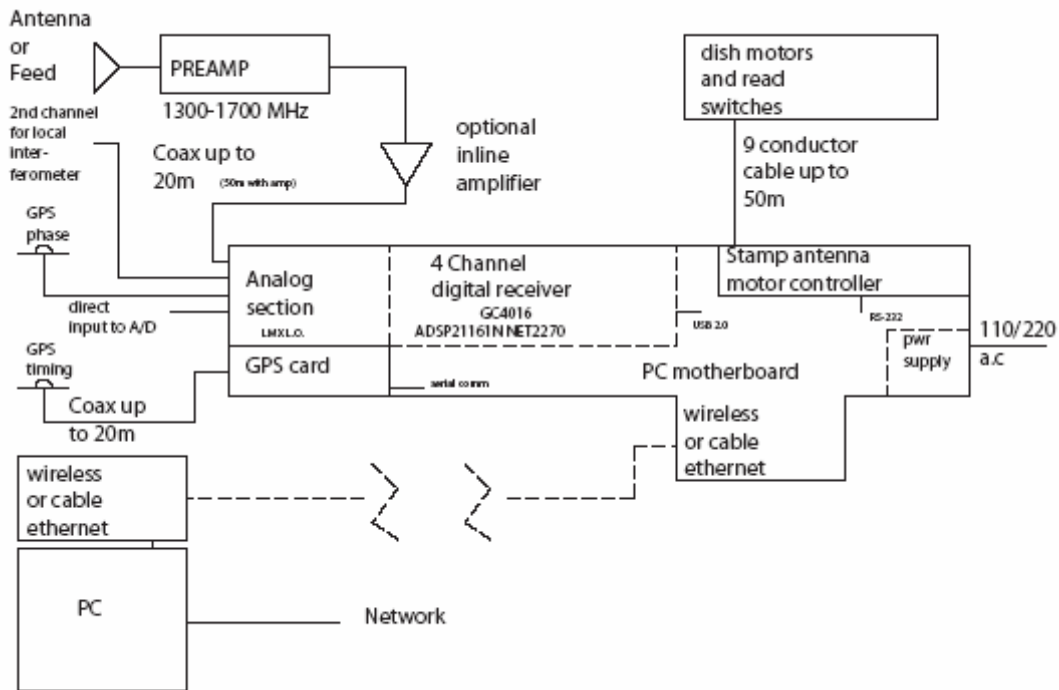

Figure 6 Block Diagram of SRT receiver. For VLBI Mode, the PC in the lower left corner connects remotely to 2 or more SRT receivers at the same time.

Software Correlation

Software correlation involves several steps. We perform geometry calculations to identify the baseline between the antennas and then project that baseline depending on the location of the object in the sky (SRT Memo #018). This geometry also allows us to calculate the a priori delay which allows us to search a smaller delay space later in the calculation.

First, the data are correlated using the a priori number of integer shifts based on the geometry calculations:

$$\rho_{xy}(\tau) = (1/N) \sum_{t=0}^{t=N-1} x(t) y(t + shift - \tau)$$

<div align="right">**Equation 1**</div>

With x(t) representing the clipped data from one antenna, y(t) representing the data from the second antenna, *shift* representing the integer number of shifts of 125 ns (*shift* = (pre-computed delay)/125), and τ in nanoseconds

The clipped data (x(t) and y(t)) is created when the SRT records the signal inputted to the system from the feed. There is a threshold halfway between the maximum input signal and the minimum input signal. If the input is below the threshold, a -1 is recorded, and if the input is above the threshold, a +1 is recorded. The specifics about how this quantized correlation is restored to a continuous function is explained in Van Vleck 1966. Next, we restore the normalized continuous correlation function from the 1-bit correlation using Van Vleck correction:

$$R_{xy}(\tau) = \sin\left((\pi/2)\rho_{xy}(\tau)\right)$$

<div align="right">**Equation 2**</div>

With $\rho_{xy}(\tau)$ defined as in Equation 1.

This continuous correlation function is also known as the delay function. In order to integrate some number of samples together to obtain fringes, the cross-correlation function needs to be transformed into frequency space, the Fourier conjugate of delay space. In frequency space, the cross-spectral function does not have any dependence on the delay τ.

This continuous cross-correlation function is Fourier Transformed to obtain a cross-spectral function which is used to integrate over some number of samples.

$$S_{xy}(w) = \int R_{xy}(\tau) e^{-2\pi i w \tau} d\tau$$

<div align="right">**Equation 3**</div>

$$S'_{xy}(w) = S_{xy}(w) e^{-i(w\Gamma + \phi)}$$

<div align="right">**Equation 4**</div>

where $w\Gamma = 2\pi kF/M$, M is the size of the FFT used to create the cross-spectral function, F is the fractional delay in units of the sample period, and φ is the fringe rotation phase in radians

If, instead of looking at the delay function, we want to look at the spectrum of the data across the bandwidth, the cross-spectral function S'$_{xy}$(w) will produce a value for the radio signal at each frequency in the bandwidth for the time slice we are currently examining. The data are integrated by summing S'$_{xy}$(w) for consecutive time slices. S'$_{xy}$(w) can be calculated for each time point in the sample, and so by outputting this function for each time point, an intensity at each (frequency, time) pair can be plotted to produce the spectral graphs seen below.

After integrating we create a delay function by Fourier Transforming from frequency space back into delay space:

$$D(\tau) = \sum_{0}^{M-1} S_{xy}(w) e^{i2\pi w\tau/(2M)}$$

<div align="right">**Equation 5**</div>

This delay function is used to compute the normalized correlation fringe amplitude, residual delay, and residual phase of the data. To improve the coherence time of the data, we perform a first order fringe rate search using a search space of four times the

Nyquist sample rate for the user selected search frequency width. The different results for fringe amplitude are stored in bins, and then for each integrated sample the bin with the maximum amplitude is selected and corresponds to that sample's fringe rotation rate. Parabolic interpolation is used between the data points to better estimate the value of peak correlation (See SRT Memo #019 & #020).

As mentioned previously, the first order fringe rotation search used in this version of the software correlator allows us to integrate for up to 7 seconds. This coherence time is limited by a combination of the software and the hardware. The software limitation results from the use of discrete steps when performing the fringe rotation search; however, the hardware limitations outweigh the software limitation. The timing variation induced by temperature variations around the GPS unit do not necessarily follow a linear path, and in particular, may drift forwards and backwards within a single integration period, which does not allow a single linear rotation term to properly fit the true rotation. While it is possible to account for these unusual variations in rotation, the computation complexity makes these computations infeasible at this time.

Calibration from External Data

In some situations, external data can be used to rescale the normalized results into a known flux unit such as Janskys (1 Jansky (Jy) = 10^{-26} W m^{-2} Hz^{-1}) or SFUs (Solar Flux Units, 1 SFU = 10^4 Jys). The most obvious example of this type of calibration is studying the Sun. Many Observatories around the world record the flux density of the Sun at various frequencies. One of the common frequencies reported is 1415 MHz, a frequency in the band used by the Small Radio Telescopes.

Once we reconstruct the normalized signal, we can use information known about the elements of the interferometer and the source to restore the flux density of the original signal. The normalized correlation, ρ_{12}, is related to the antenna temperatures as shown where $T_{fi} + T_{si} + T_{ri}$ is the total antenna temperature of antenna i:

$$\rho_{12} = \sqrt{\frac{T_{f_1}T_{f_2}}{\left(T_{f_1}+T_{s_1}+T_{r_1}\right)\left(T_{f_2}+T_{s_2}+T_{r_2}\right)}}$$

Equation 6

Where T_{f1} = antenna temperature of the flare on antenna 1, T_{s1} = antenna temperature of the sun on antenna 1, T_{r1} = receiver noise on antenna 1, and similarly for antenna 2. With:

$$T_f = \frac{A_{eff}F_f}{2k_B}$$

Equation 7

Where A_{eff} = effective aperture of antenna, F_f = flare flux density, k_B = Boltzmann constant. We can use this equation with the known flux density of the source and the known or estimated effective aperture of the antenna to estimate the antenna temperature for that source. Next, we substitute into Equation 6 for T_{f1} and T_{f2} to solve for F_f in units of W*m^{-2}*Hz^{-1} giving:

$$F_f = \frac{\rho^2 k_B}{1-\rho^2}\left[(T_1+T_2)\pm\sqrt{(T_1-T_2)^2+\frac{4}{\rho^2}T_1 T_2}\right]$$

Equation 8

With all variables defined as above, and:

$$T_i = \frac{T_{s_i}+T_{r_i}}{A_{eff_i}}$$

Equation 9

One can then look more closely at the two terms in Equation 8. If the square root term is greater than $(T_1 + T_2)$ then only addition is applicable because the flux must always be positive since we are receiving a signal. The inequality:

$$(T_1+T_2)<\sqrt{(T_1-T_2)^2+\frac{4}{\rho^2}T_1 T_2}$$

Equation 10

can be reduced to checking if $1 < (1/\rho^2)$ which is always true because ρ is defined to be always less than unity, so only addition is applicable.

This method will determine the flux density of a flare on the source. Due to the fact that we are using external data to determine the flux density and antenna temperature of the source, our results are not completely accurate. The sun in particular can vary significantly in flux density over the course of the day. Most of the activity seen to date with the SRT interferometer are "microbursts" with strength on the order of one percent of the total power emitted by the sun, so using slightly inaccurate values for the flux density of the sun could cause the calculated flux density of the flare to be off by a significant amount.

Background on the Sun

The sun is a very hot topic of research; however, only certain parts of the sun are regularly studied. Many research groups dedicate full time effort into studying the sun, such as the Japanese *Yohkoh* satellite and the United States's *GOES* series satellites (operated by the Space Environment Center of the National Weather Service). These particular efforts are dedicated to studying the sun in the X-ray and gamma ray frequency bands. Other efforts, such as various radioheliographs around the world, constantly look at the sun at many different frequencies from 1 Hz up to several tens of GHz, but these efforts have limited sensitivity. The instruments with the best sensitivity are dedicated primarily to looking at other sources of astronomical interest such as distant galaxies. In this study we are lucky to have continuous access to a high resolution interferometer to look at activity on the sun.

Many people have previously studied the sun at frequencies lower than 700 MHz. These studies have discovered 5 major types of radio burst activity where a burst refers to an enhancement of radio activity above the quiet sun levels for some period of time. Of particular interest here are type III bursts. Type III radio bursts are a "short" duration strong enhancement that drifts over a range of frequencies. Typically, the frequencies go from higher to lower over the course of the burst, which can be explained by the current theory of the creation of this type of activity. Experts believe that Type III bursts are caused by plasma excitation from a stream of energetic electrons traveling upward in the corona of the sun. The resonant plasma frequency goes down as the density and temperature of the plasma reduces causing the downward frequency drift at average rates of > -2 MHz/s. These type III bursts are created by the conversion of Langmuir waves into transverse electromagnetic waves. The exact process by which this conversion occurs is still disputed, but most Type III bursts have a frequency of $2\nu_{pe}$. The standard Type III burst only occurs at frequencies as high as a few hundred MHz.

Originally, type III radio bursts were thought to be non observable in the frequencies above a few hundred MHz because free-free absorption would consume the waves long before they could escape from Sun. High frequency Type III radio bursts are known to exist; however, this type of burst is not frequently studied. Typically, these high frequency bursts are seen starting at a frequency greater than 1 GHz and have a "reverse drift" meaning that these waves are created by electron beams accelerating downwards in the solar corona. It is still unclear why these


Figure 7 Example image taken with Yohkoh HXT. Lower right image shows the double footprint typically seen in hard x-ray events caused by the electrons following two side of a magnetic field loop. Image from Yohkoh website.

14

bursts are not consumed by free-free absorption, but possibly creation through harmonic plasma radiation reduces the effective distance to exit Sun.

A small number of studies have used instruments such as the VLA to observe the Sun; however, these studies have been limited to observations during one or two days. T.S. Bastian first discovered short duration radio activity on the Sun in the 1400 MHz band in the early 1990's. He classified the small magnitude, short (~10 seconds) bursts as "microbursts", and suggests that more study is needed to better understand these bursts and their relation to other activity on the Sun. Bastian observed microbursts centered around active regions on the Sun with an angular size of 15" - 30". Through his non-exhaustive examination of 11 microbursts, Bastian observed total flux ranging from 0.06 to 3.8 s.f.u. and notes that these bursts may be composed of many shorter duration bursts because of the instrumental limitations of the VLA setup used, which allowed a minimum integration time of 10 seconds.

Other groups study the sun at much higher frequencies, such as the *Yohkoh* and *GOES* projects. These groups have studied the cause of X-ray bursts on the sun. Their results lead to the conclusion that X-ray flares are caused by streams of energetic electrons following magnetic field lines in the corona. They believe that the X-ray flare is caused by the sudden slowing of these electrons when the electrons reach the end of the field line. Typically, this sudden slow down occurs at the interface between the corona and the chromosphere. When observing an X-ray flare, one can trace the magnetic field loop by careful examination of the X-ray flare source variation with energy and time. The highest energy X-rays will be produced by a double footprint at the base of the magnetic loop. One footprint is always stronger than the other which allows one to infer which side of the magnetic loop contained the original source of the energetic electrons.

A few groups have studied correlations between the different frequency activities on the sun. Many large X-ray flares are accompanied by a Type III Radio burst because the event that excited electrons that cause the x-ray flare also excites electrons in the upward direction, which travel through a part of the corona that emits radio waves at a frequency less than 1000 MHz. Most groups that have looked at connections to radio bursts have used radio burst detectors that study a few tens of MHz up to a few hundreds of MHz. Others have looked at even lower frequencies. The next groups that have studied a connection to X-ray flares have drawn conclusions about microwave solar activity at frequencies in the tens of GHz or higher. In this microwave range, experts believe that the excited electrons that later cause an X-ray flare travel downwards through a section of the corona that emits radio waves at microwave frequencies.

Upward Beams

$n_e^{acc}=3\ 10^9\ cm^{-3}$

Acceleration Site

$\nu^{III}=500$ MHz

III

RS

Downward Beams

$\nu^{dm,1}=1$ GHz

MW

DCIM

$n_e^{dm,1}=10^{10}\ cm^{-3}$

Chromospheric Evaporation Front

SXR

$n_e^{SXT}=10^{11}\ cm^{-3}$

$n_e^{dm,2}=5\ 10^{10}\ cm^{-3}$

$\nu^{dm,2}=2$ GHz

TIME

FREQUENCY

HXR   HXR
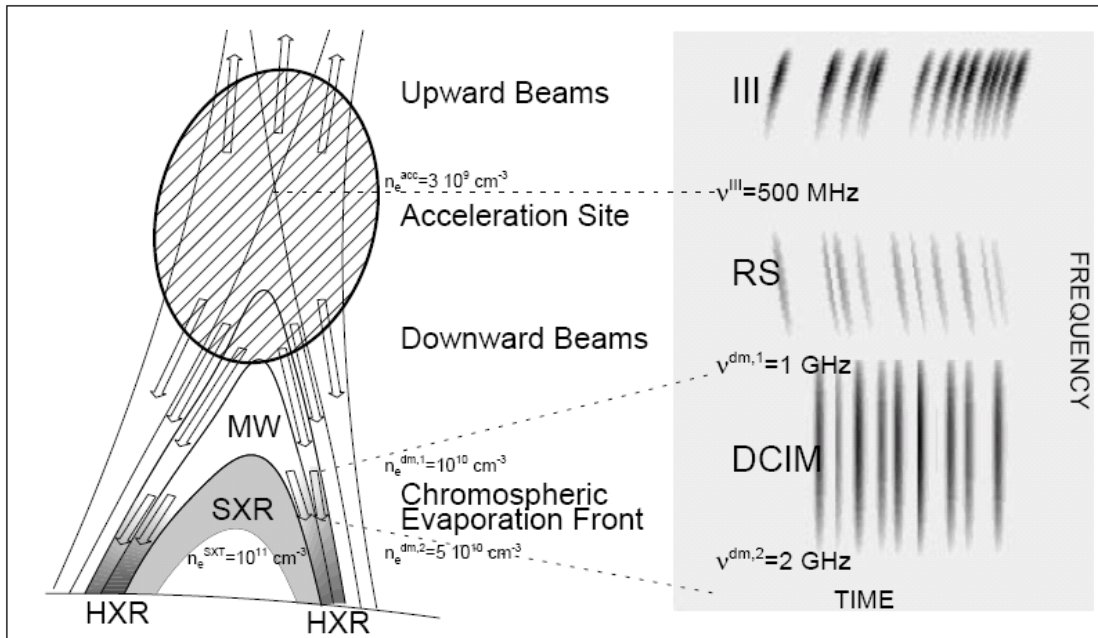
Figure 8 After years of solar study, experts have developed a model of how a wide range of solar activities are interconnected. A single site of acceleration can send electrons upwards and downwards in the corona of the sun. Arrows indicate the direction of the electron motion and the areas where radio emission can occur. Lowest frequencies are at the top of the image. Highest frequencies occur at the bottom of the image. If electrons are accelerated away from the center of the sun, a standard type III radio burst that drifts downwards in frequency will occur. Standard type III bursts occur at frequencies below 500 MHz most of the time giving rise to the type of structure shown next to the III on the upper right corner of the image. The darkness of the plot indicates the intensity of the signal, so type III bursts are strong and easy to detect. When electrons are accelerated downwards in the corona, several different things can occur. First, a reverse slope type III burst can occur. These reverse slope bursts drift upwards in frequency with time. It took many years before these bursts were observed because of their weaker intensities thought to be caused by free-free absorption as the signal tries to leave the sun. If the electron beam interacts with the Chromospheric Evaporation Front, decimetric bursts (DCIM) can occur. These bursts occur after a reverse slope type III and have a time signature that looks as shown in the lower right on the figure. HXR indicates the location of Hard X-Ray events, SXR for Soft X-Ray events, and MW for sources of microwave activity. As the electrons reach certain areas of the magnetic field lines, different types of high frequency events occur. Generally, these high frequency events will happen in order as the electron beams reach certain parts of the magnetic field lines as shown: microwave emission (MW) comes first, Soft X-ray emission (SXR) comes next, and Hard X-ray emission (HXR) comes last as the electrons screech to a halt as they collide with the chromosphere. Another important feature to note is the physical location of the high frequency activity. Microwave and Soft X-ray activity primarily occur at the top of a magnetic field loop. Hard X-ray activity on the other hand occurs at the base of the magnetic field loop. In nearly all cases, images of hard X-ray activity will produce a "double footprint" outlining the two base points on the chromosphere that represent the base of the magnetic field loop. In various locations on the figure, the electron number density required to produce each type of activity is listed. In all downward accelerating cases, the same electrons can produce every type of event seen. Image from Bastian, Benz, and Gary, Annual Reviews 1998.

One study of particular importance to phenomena observed here discusses millisecond spikes in the 1300 to 1500 MHz band. Dąbrowski et al. used a spectrometer designed for pulsar observations to look at the sun for 357 observing days. During this time, 13 groups of millisecond spikes were observed. This group analyzed their results and conclude that there are two different types of millisecond bursts, "bursts with internal structure" and "bursts without internal structure". Millisecond spikes are defined to be radio bursts shorter than 100 ms. According to the statistics presented by Dąbrowski, both types of bursts observed have a wide range of lengths and frequency drifts with significant overlaps in the ranges. A "spike without internal structure" consists of a single point of increased flux limited in time and frequency. "Spikes with internal structure" show several internal minimums and maximums. It is very possible that the bursts without internal structure are unresolved by their system. In their study, Dąbrowski et al. find bursts drifting in both directions in frequency, with each burst having its own frequency drift. The frequency resolution of their data is limited to 3 MHz wide bins, and they integrate their data for 0.8ms to 4 ms. The somewhat ambiguous description of the experimental setup and data analysis provided in the paper makes it unclear exactly what integration times are used.

Only a small percentage of the studies of the sun make reference to the frequencies between these more prominently studied bands. Most instruments dedicated to the 1-2 GHz frequency band spend almost all of their up time looking at other astronomical phenomena instead of the sun.
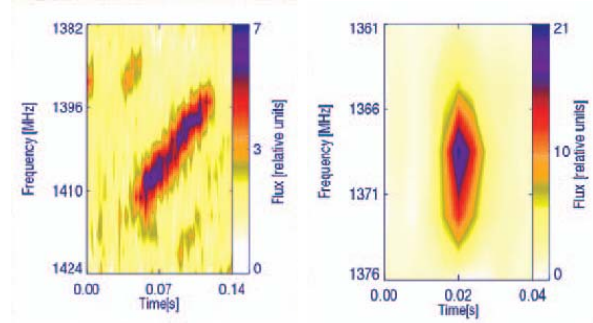
Figure 9 Left: sample Burst with Internal Time Structure. Right: sample Burst without Internal Time Structure. Pay special attention to the time and frequency scales on each plot. Images from Dąbrowski et al. 2005

Data Used

For this analysis I used data from several different sources. First and foremost is the data from the SRT interferometer. Next, I obtained data from the GOES Satellites through the online database maintained by the SEC of NOAA. Additionally, I obtained freely available data from the Radio Solar Telescope Network (RSTN).

The SRT interferometer recorded for 10 days during September 2005 in addition to a handful of days scattered across July and August 2005. We use integration times ranging from 512 microseconds to 0.4096 seconds for all SRT interferometer data in this paper. For most of the time we recorded, the Sun was very active, producing a few X class solar flares (very rare) and at least a dozen M class solar flares (not quite as rare). We observed one X class flare and about half a dozen M class flares. These limitations were imposed by the SRT design and by the rotation of the Earth during the periods of observation. We also observed periods with total solar X-ray activity 1-2 orders of magnitude weaker that we reference as a comparison to impress the significance of the significant features analyzed herein.

The GOES Satellites orbit Earth in a geosynchronous orbit. At least one satellite is always able to observe Sun. The instrument of interest to this project is the Space Environment Monitor that is used to calculate the total solar flux at two

different X-ray wavelength bandpasses (1-8 Angstroms and 0.5-4 Angstroms). The data for the total solar flux is made available from the SEC website (http://www.sec.noaa.gov) with integration times of 1 minute or 5 minutes. For this project, I used the one minute integration data to have closer correspondence to the half second integration data from the SRT interferometer.

The Radio Solar Telescope Network has 4 sites worldwide that constantly monitor Sun at 8 different frequencies ranging from 245 Mhz to 15.4 GHz. The highest time resolution data available from RSTN are 1 second integration, which is very good for using to compare with the SRT interferometer data. These data are available from NOAA online from the NGDC (National Geophysical Data Center http://www.ngdc.noaa.gov/ngdc.html).

SRT Data

Most of the time while observing Sun with the SRT interferometer, nothing of significance is seen. Regardless of what the Sun is doing, noise fringes will be seen by the interferometer. The primary criteria we use to determine the significance of a
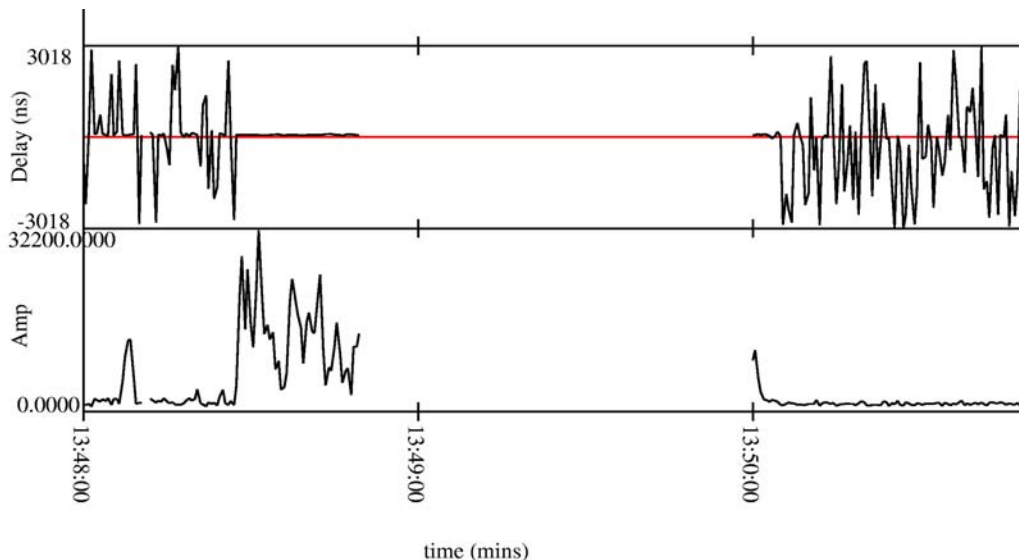
Figure 10 Example of SRT fringes indicating a signal. This particular observation is from August 4, 2005. The upper plot shows the residual delay. The lower plot indicates the fringe amplitude in Janskys. When the event starts, suddenly the residual delay drops to nearly zero and stays around zero until the end of the event. At all other times the residual delay appears to be almost random. The SRT was not recording from a little bit before 13:49 until 13:50. The red line across the delay window is the zero residual delay reference.

signal is the residual delay. Due to the geometry of the positions of the antennas, we can precompute the expected delay between the two signals arriving at the antennas. After adjusting for the precomputed delay, a residual delay search is performed to find the strongest fringe within a given range of possible delays. If the strongest fringe is located at, or very close to, zero residual delay for several consecutive readings, we determine the reading to be of significance rather than just random noise. In most cases studied closely here, it is fairly obvious that a legitimate signal is observed because of the sudden change in fringe amplitude (the amplitude doubles or more) and the extended duration of the signal. In many other cases, the signal is not as

18
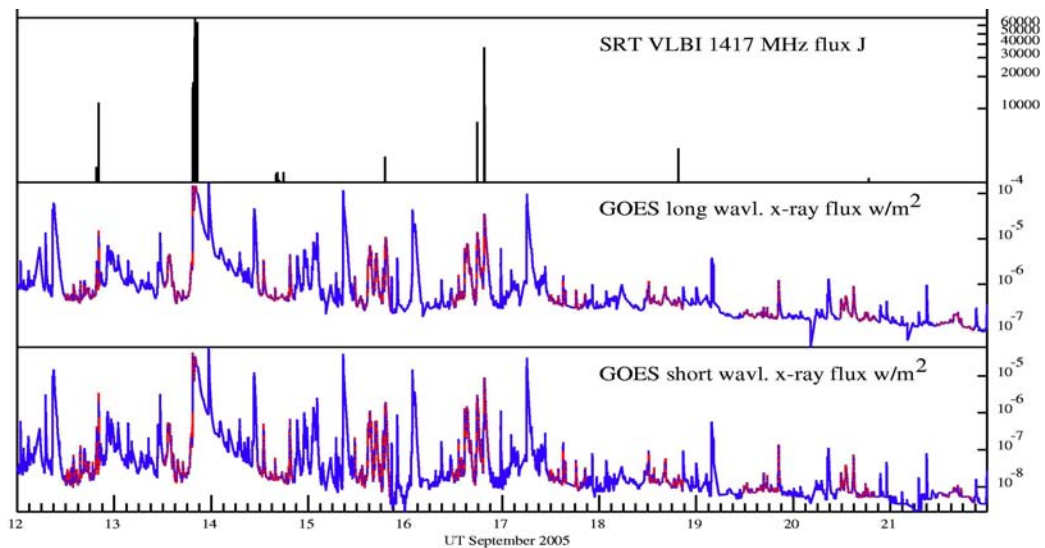
Figure 11 Overview of September 2005 data. The top plot shows a logarithmic plot of the SRT data filtered to show only very large events or events with greater than 3 consecutive readings with a residual delay less than ±200 ns. The middle and lower plots show total solar X-ray flux recorded by GOES 12 at two different wavelengths. On the lower two plots, red line segments indicate times when the SRT was recording and blue line segments indicate times when the SRT was not recording.

prominent. I visually cataloged approximately 2,100 events seen during the September 2005 recording period in the hopes that some trends would emerge to identify different types of burst activity observed. Based on the data listed with each burst in the current version of the catalog, no obvious trends appear; however, it is possible that with added feature information some identifiable pattern could emerge.

I concentrated my efforts on understanding 8 major burst groups. These are the most significant groups of bursts observed with the SRT interferometer in this dataset. Most of these groups consist of one or more impulsive spike with some form of exponential decay. One burst group in particular defies simple classification; the burst group on day 256 lasts nearly non-stop for over an hour at the end of our recording session with some highly impulsive bursts intermingled with much slower rising enhancements. Within this burst group there are some very highly impulsive, short duration bursts that may never have been resolved by any groups before.

Table 1 Listing of all observing time used during this analysis for in depth study. Prior to September observations are not constantly occurring.

Date 2005	Start Time UT	Stop Time UT
2 Aug	13:21	19:18
4 Aug	13:22	20:02
12 Sep	11:40	20:30
13 Sep	12:10	20:30
14 Sep	11:20	20:20
15 Sep	11:30	20:40
16 Sep	11:30	20:40
17 Sep	11:30	20:40
18 Sep	11:30	20:40
19 Sep	11:30	20:40
20 Sep	11:30	20:40
21 Sep	11:40	20:50
22 Sep	11:40	20:50

Analysis

This section will first present an overview of the analysis approach taken. After the overview, I will look more closely at each major event, presenting all data for that specific event in one place.

First Look at the Data with X-rays

After recording for 10 days in September, I started to analyze the data. From my analysis of several events in July and August, I believed that an integration time of
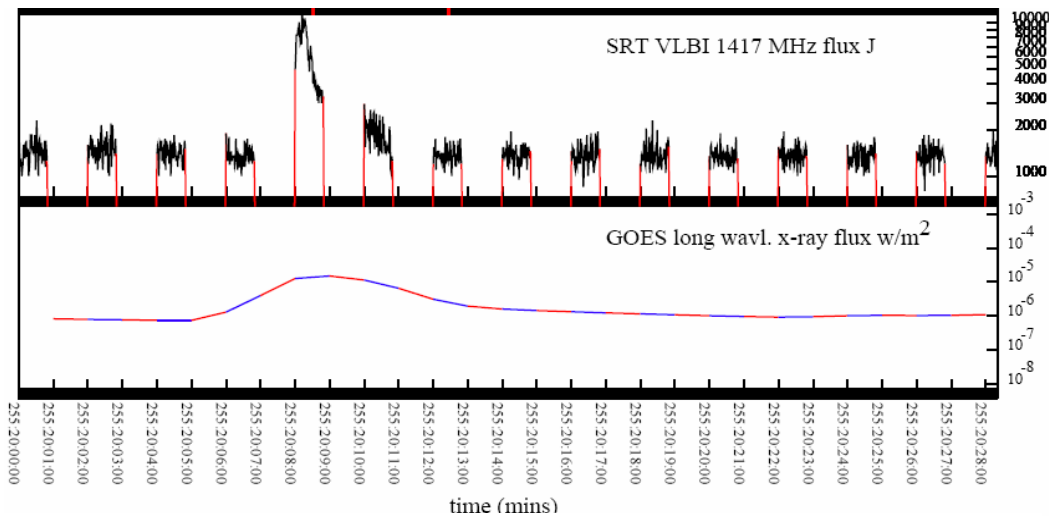

Figure 12 Burst observed on 12 September 2005 with associated M-class X-ray flare. The red vertical lines on the SRT plot indicate the start and stop of each recorded block. The block starting at 20:08 UT shows the end of the impulsive rise of the radio burst. The exponential decay of this event can also be seen starting just after 20:08 UT and continuing until at least 20:11 UT. On the lower plot, blue segments correspond to when the SRT is recording, and red segments correspond to when the SRT is not recording.

approximately half of a second would be a good place to start examining this new data. Upon first look, I noticed what looked like it could be a correlation between significant radio events and X-ray bursts observed by the GOES total solar flux readings. While not all X-ray events appear to have an associated burst observed by the SRT interferometer, nearly every significant burst observed by the SRT interferometer appears to have an associated X-ray flare. More specifically, for every M-class or larger X-ray flare that occurs while we are observing, the SRT Interferometer records a burst. In some cases, particularly larger C-class X-ray flares, a radio burst is observed, but for the remaining C-class or smaller X-ray flares, no significant burst is observed.

Looking more closely, most of the radio events seen do not last for very long. With one exception, the major events observed last from a few seconds to a few minutes at most, while the associated X-ray flare is visible for several minutes up to several hours. In every case of M-class or larger X-ray flare, the radio event appears at or very close to the peak of the X-ray activity. For the events a few minutes in duration, the radio burst rises very impulsively but then decays exponentially.

The most interesting radio burst recorded during September 2005 occurred during the X-class solar flare that started at 19:22 UT. The sun moved past the limits of our observation at approximately 20:36 UT. We see nearly continuous radio activity for that entire time. Within this event there could be several different activities occurring to produce the different shapes over time.

X-Ray Burst Association with SRT Data
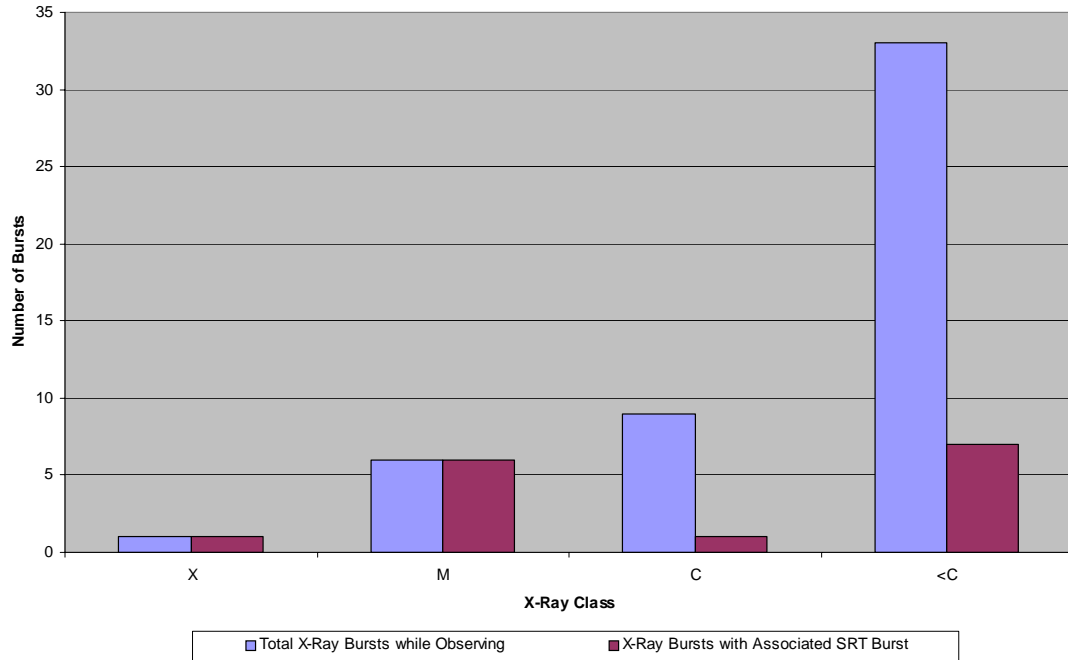
Figure 13 Chart showing total number of each class of X-ray burst while observing and number of X-ray bursts with an associated significant SRT burst. Every significant SRT burst seen to date has an associated X-ray flare of some variety. Classification of <C class X-ray bursts as actual bursts is slightly subjective for the purpose of this paper. Any increase in GOES flux is treated as a burst whereas technically according to NOAA, the flux must increase for a certain number of readings to be truly classified as a flare.

Table 2 Details about each flare observed with associated radio burst info. For ≥M class, the subcategory is also given (bigger number subcategory means bigger flare). I studied the dynamic spectra of each peak visible at 512 μs integration.

X-ray Burst Time (UT)	X-ray Class	Peaks Visible at 512 μs Integration	Frequency Structure at short integration	Single Radio Peak
11 Jul 2005 13:18	B			Unknown
12 Jul 2005 16:18	M 1.5			X
2 Aug 2005 18:27	M 4.2			X
3 Aug 2005 13:57	M 1			
3 Aug 2005 18:09	B			X
4 Aug 2005 13:50	B			
4 Aug 2005 17:35	B			X
12 Sep 2005 20:06	M 1.5			X
13 Sep 2005 19:22	X 1.5	11	X	
14 Sep 2005	B			X
15 Sep 2005 19:00	C			X
16 Sep 2005 17:40	M 1.4			
16 Sep 2005 19:30	M 3.5	5		
18 Sep 2005 19:30	B			X
20 Sep 2005	B			X

These X-ray plots very quickly became deceiving because of the disparity in time resolution between observations with different instruments. The highest time resolution data we obtained from GOES consisted of one minute integrations, while at this point all of the SRT data used an integration time of 0.4096 seconds. My next thought was to find higher time resolution GOES data to see if any of these X-ray flares contained finer structure that in some way corresponded to the structure we observed in the SRT data. We never tested this theory because no matter who we contacted, we never received a response about higher time resolution GOES Solar Flux data.

Across the Radio Frequencies

As mentioned earlier, standard Type III solar bursts are not generally seen at frequencies higher than a few hundred megahertz; however, several studies have examined these higher frequency Type III bursts that extend as high as 3 GHz. Typical microwave solar emission is generally seen at frequencies higher than 5 GHz, but is occasionally observed at frequencies as low as around 1 GHz. Given this overlapping region, I wanted to determine which phenomena I observed to be able to build a more accurate picture of the cause of the radio bursts I am seeing.

I decided to approach this problem by plotting RSTN data. The RSTN data source is a good choice for several reasons: time resolution of 1 second is freely available on the internet, a wide range of frequencies are available both above and below our observing frequency, and single dish observations at a frequency very close to ours is available for comparison. On the flip side, the RSTN data present some challenges as well: very little user support is provided for this data. I could not find a single email address to contact to get questions answered about the data. The network does not publish details about what equipment is used to make the observations or what processing is performed on the data except for a one line description stating that all measurements are corrected to 1 AU.

The pros and cons being what they are, I proceeded to look at data from RSTN plotted with the SRT data, and I plotted the X-ray data for reference. Upon examination of these plots, I found that most of the events observed by us also have higher frequency components. In one case, the only frequency to see activity is the 1415MHz recording. In one other case, every frequency recorded shows some level of activity at some point during the SRT event.

At this point I needed to stop and reassess what to do. Up to this point, we believed that the events we observed were very small and would not be seen by a single dish observation unless that dish is very large. The fact that the RSTN single dish observations showed very similar data at 1415 MHz caused me to question what benefit the SRT interferometer provided that the RSTN data could not provide.
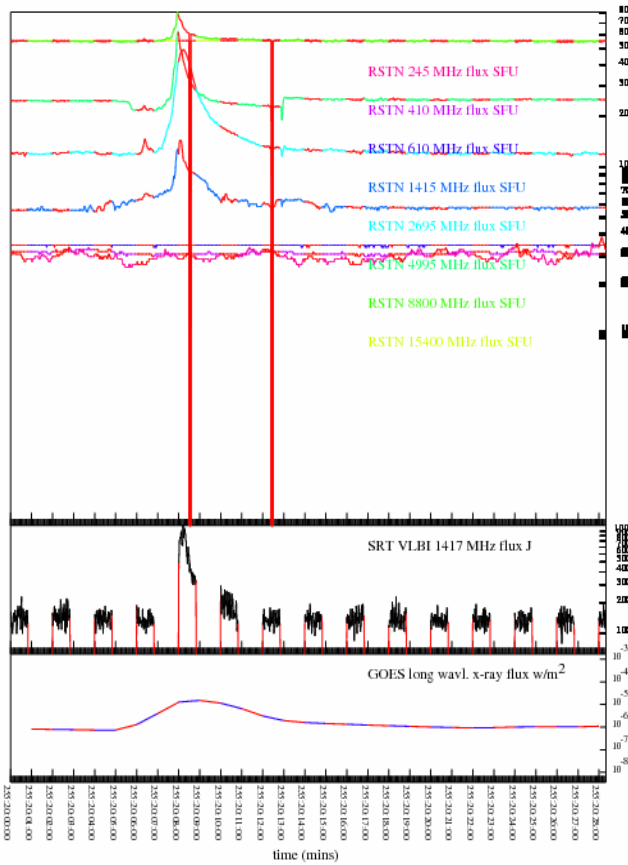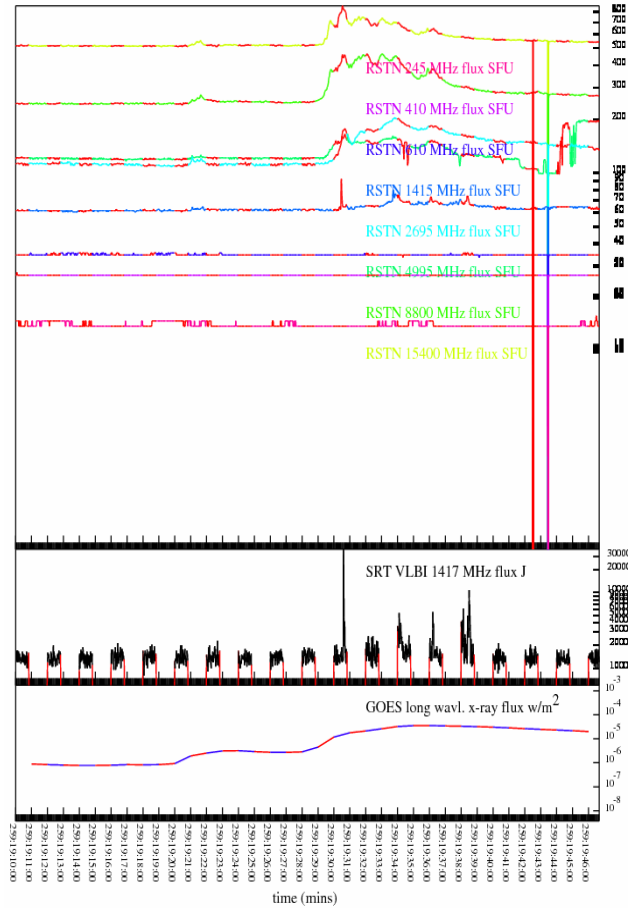
Figure 14 Two events plotted with RSTN data. The bottom subplot shows the GOES data at one wavelength for reference about when the X-ray flare occurs. The next subplot up shows the SRT interferometer data on a logarithmic scale. The red vertical lines on the SRT plots indicate the beginning and ending of each recording window. The top box has all 8 frequencies recorded by RSTN plotted in different colors. Frequency increases as the lines get closer to the top of the image. Red segments on the RSTN data indicate times when the SRT was recording. The vertical lines in the RSTN plots indicate times when there is no RSTN data. The lines are artifacts of the plotting package. The medium blue 1415 MHz RSTN data line shows very similar results as the SRT data for the times when the SRT is recording. See below for a more in depth examination of these events.

25

High Time Resolution

The first benefit realized by the SRT interferometer is arbitrarily small time resolution. Using VLBI mode interferometry data, we can recorrelate the data using a shorter integration time to see if any events seen as a single bump at longer integration times actually contain more than one bump.

As I recorrelated with shorter and shorter integration times, most of the events were swallowed by the noise. An event becoming less visible on shorter integration times just means that the signal is only a little bit stronger than the background at the shorter time scale; however, upon adding up many of these little bits, a signal that looks much stronger than the noise around it is obtained.

A few events did stay visible and strong at the shorter integration times. In each of these cases, a single event observed by the RSTN antenna turned into a collection of events on the SRT interferometer; however, to see these events requires massively expanding the SRT data to see the distinct peaks.

Studying these few events that remain visible led to a few questions. At this point is when I started carefully studying the paper by Dąbrowski et al. about millisecond bursts. Between the data in this paper and our other knowledge that most bursts seen on the sun drift in frequency with time, I decided next to look at the cross power spectrum around these events still visible on short integrations.
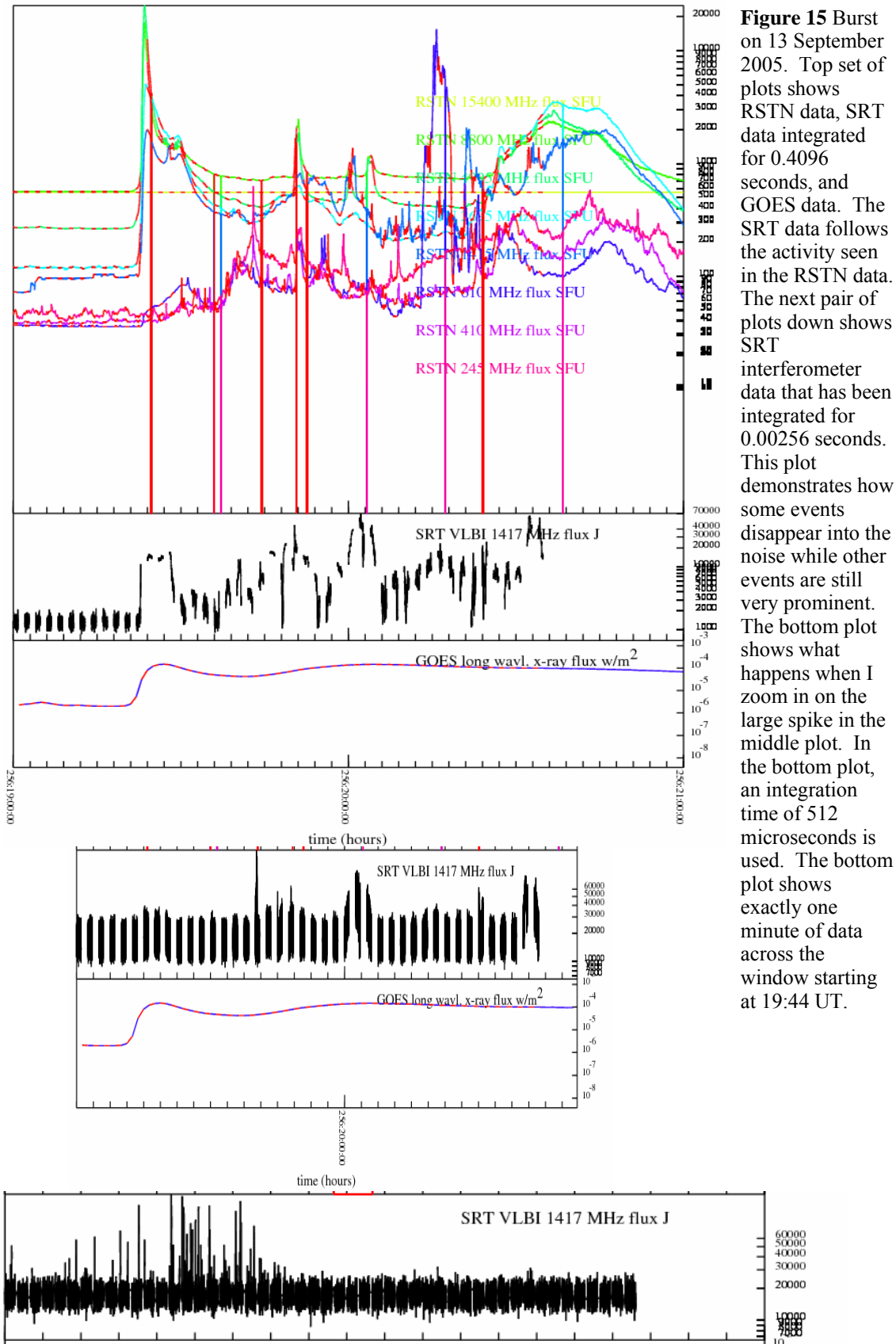
Figure 15 Burst on 13 September 2005. Top set of plots shows RSTN data, SRT data integrated for 0.4096 seconds, and GOES data. The SRT data follows the activity seen in the RSTN data. The next pair of plots down shows SRT interferometer data that has been integrated for 0.00256 seconds. This plot demonstrates how some events disappear into the noise while other events are still very prominent. The bottom plot shows what happens when I zoom in on the large spike in the middle plot. In the bottom plot, an integration time of 512 microseconds is used. The bottom plot shows exactly one minute of data across the window starting at 19:44 UT.

Plot starts at 19:44 UT on 13 Sep 2005. Tick marks every 3 seconds. Duration 1 minute.

27

Digital Spectroscopy

Digital spectroscopy turns out to be very simple to do with the SRT interferometer. As part of the correlation, the cross-correlation function (Equation 2) is Fourier Transformed to a cross-spectral function to perform integration. To examine the spectrum of the data, one simply outputs the integrated cross-spectral (Equation 4) function instead of continuing by Fourier Transforming the cross-spectral
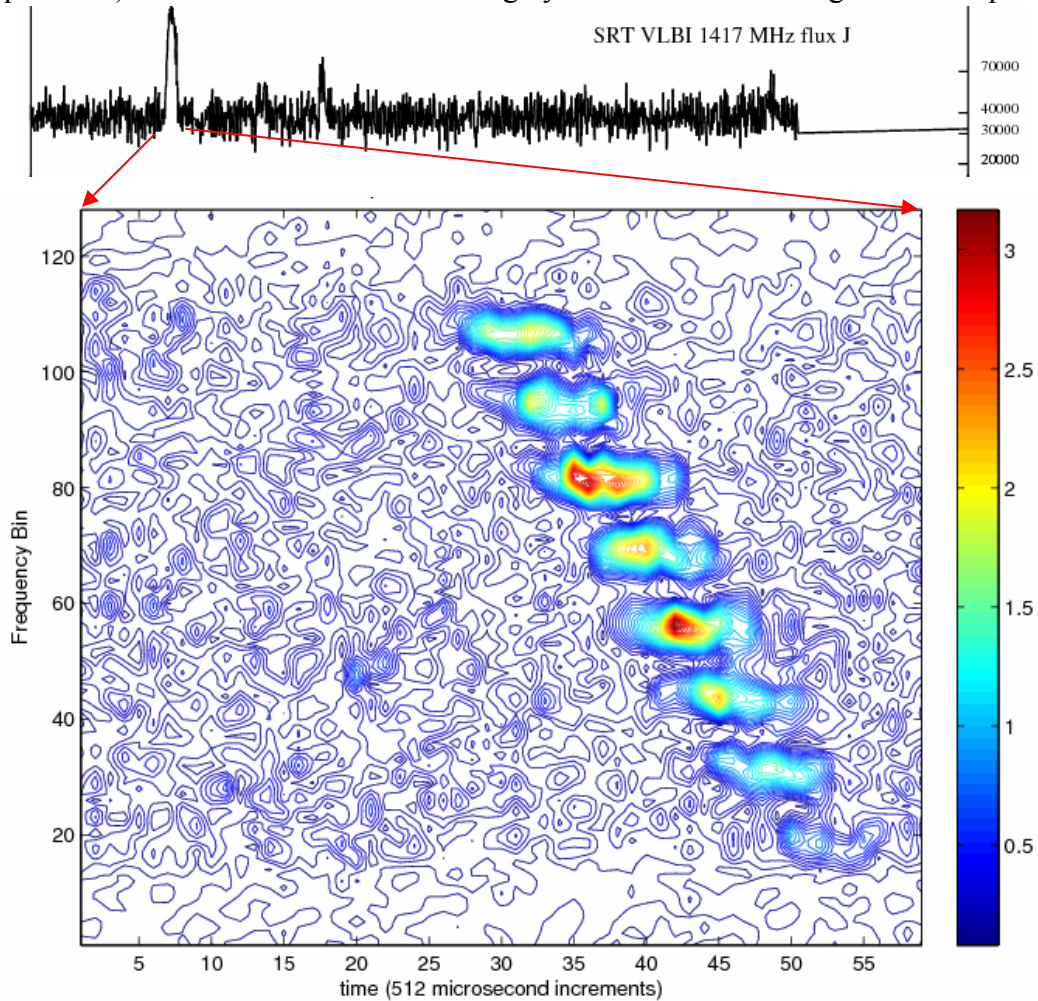
Figure 16 Burst at 13 Sep 2005, 19:44:13.14. The upper plot shows the total flux observed by integration of the entire bandwidth of the interferometer. Across the upper plot, 1 second elapses. The lower plot shows the cross-spectral output for the large peak seen in the upper plot. Both plots use an integration time of 512 microseconds. The lower plot has frequency bins that are 31.25 KHz wide.

function to create the delay function (Equation 5).

Having only a 4 MHz bandwidth, we initially hoped to just be able to detect a drift in frequency between the top and bottom half of the bandwidth so that we could determine if these events are drifting up or down in frequency with time. When I produced the first plots, I was very surprised with what I saw. Instead of a band sweeping across our bandwidth, I found a series of defined peaks drifting across the bandwidth. In total, there are 11 known bursts with this multi-peak drift. These 11 bursts occur in a window of 20 seconds with each individual burst lasting about 15-20

milliseconds.

I next calculated the brightness temperature of one of these bursts. Starting from the Rayleigh-Jeans law:

$$I_v = \frac{2k_B T}{\lambda^2}$$

Equation 11

Where I_v is the specific intensity, k_B is the Boltzmann constant, T is a temperature, and λ is the wavelength of the radiation.

And then using the knowledge that I can get a specific intensity from a flux density by dividing by the solid angle of the beam:

$$I_v \, \Omega = S_s$$

Equation 12

I find that:

$$S_A = \frac{2k_B T_A}{\lambda^2} \, \Omega$$

Equation 13

Where S_A is the flux density at the antenna, k_B is still Boltzmann's constant, T_A is the antenna temperature, λ is the wavelength of the observation, and Ω is the solid angle of the beam.

Because we are resolving the source, it does not take up the whole beam. This means that T_A is not the brightness temperature of the source. Using the relation

$$T_A \, \Omega_A = T_S \, \Omega_S$$

Equation 14

Where Ω_S is the angular size of the source. We find that

$$T_S = T_A \, \Omega_A \, / \, \Omega_S$$

Equation 15

And

$$T_A = \frac{S_A \lambda^2}{2k_B} \, \Omega$$

Equation 16

With everything defined as above
Putting it all together and plugging in:

$S_A = 154{,}700$ Jy for a typical large peak in these drifting bursts
$\lambda = 21$ cm
$\Omega_A = \lambda^2 / D^2$ (Diameter of the antenna) $= 0.01$ rad^2 (even though it cancels out)
$$\Omega_S = \left(\frac{t \times c}{1AU}\right)^2 = (2 \text{ milliseconds} * 3E8 \text{ m s}^{-1} / 1.5E11 \text{ m})^2 = 16E\text{-}12 \text{ rad}^2$$

Gives $T_s = 1.5 * 10^{13}$ K. In this case, I have used a duration of 2 milliseconds because that is a typical length of a single pulse within the drifting burst. This brightness temperature is absurd to consider as a thermal activity, so it must be some form of coherent emission.
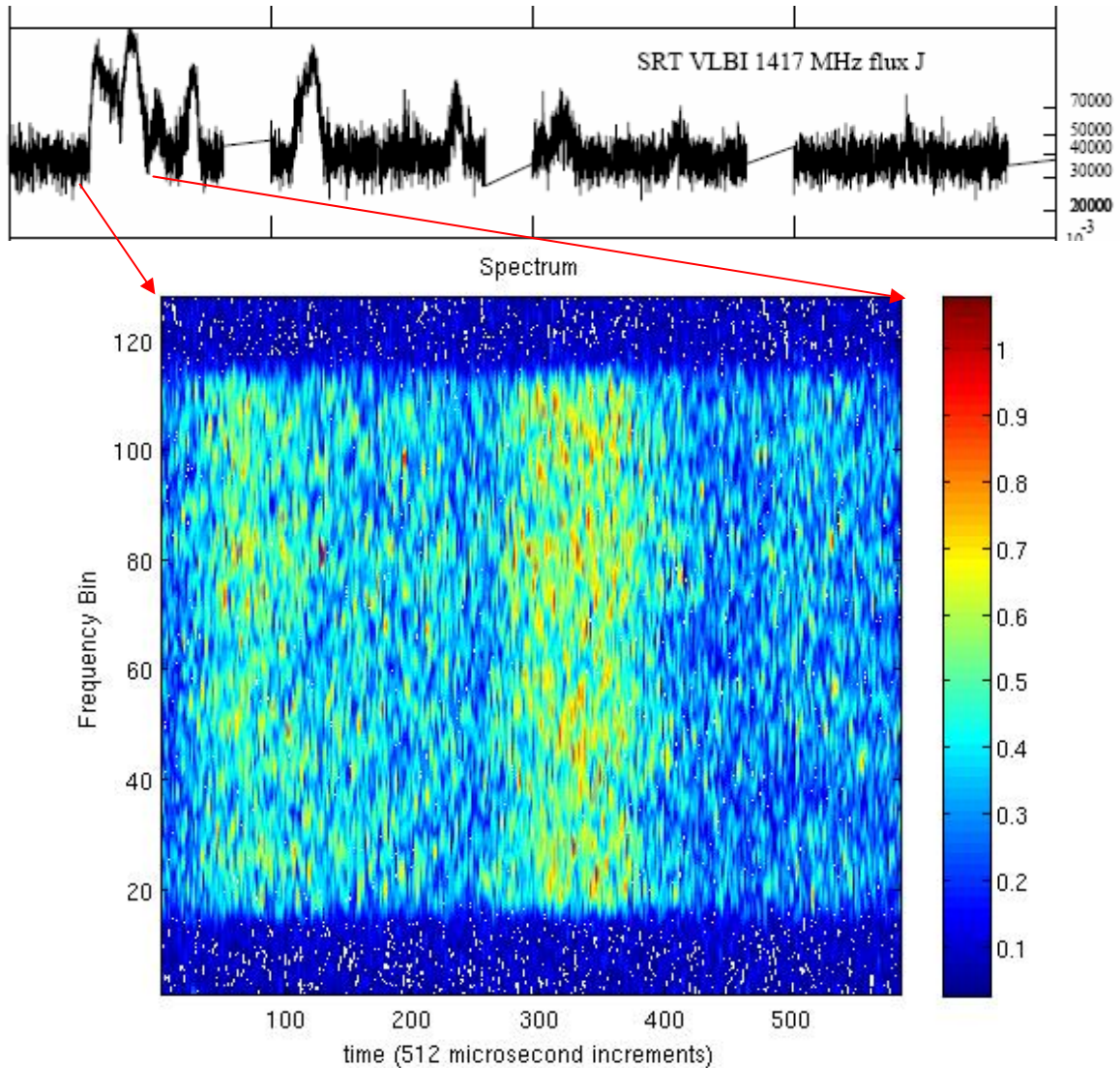
Figure 17 Burst 16 Sep 2005, 19:30:36.3 UT. Upper plot shows 4 seconds of the total fringe amplitude starting at 19:30:36 UT with markers at 1 second intervals. Lower plot shows the spectrum associated with the first two peaks on the left in the upper plot. This type of burst is not as clearly defined at the 13 Sep 2005 bursts; however, there is definitely activity present. As before, integration time of 512 microseconds with 31.25 KHz wide frequency bins.

There is one other time on a different day that still shows strong fringes at an integration of 512 microseconds. Yet another surprise arrived when I looked at the spectrum of this second event. At first glance, this set of events looks very similar to the first set of events observed on this time scale, but this time, the spectrum shows fairly uniform flux across the bandwidth with a peak amplitude of approximately one third of the peak amplitude seen in the first set of events. Following the same steps as above to calculate the brightness temperature and

S_A = 160,000 Jy (the amplitude of the second peak in Figure 17)
Duration = 50 milliseconds, Ω_S = 1*10^{-8} rad^2

We find a brightness temp T_B = 2.5 * 10^8 K

31

Individual Events

In the following sections, each major event will be discussed in detail. All information known about the event will be examined. For all events, the X-ray and RSTN data will be explored. In the cases that warrant further study, high time resolution and spectral study will be examined as well.

2 Aug 2005, 18:27 UT

This is one of the first events observed with the SRT interferometer. By looking at the association of the X-ray flare and the SRT data, we first thought about the connection between these two events. The X-ray flare is rather large, although it is still an M-class flare. With larger X-ray flares, we expect more activity across the spectrum. This event is still very visible with an integration time of 0.0128 seconds; however, by the time we reach 512 microseconds, this event is lost in the background. This event is somewhat unusual in that the SRT burst seems to have an exponential increase and then a very abrupt end. Normally, we expect the opposite to happen.
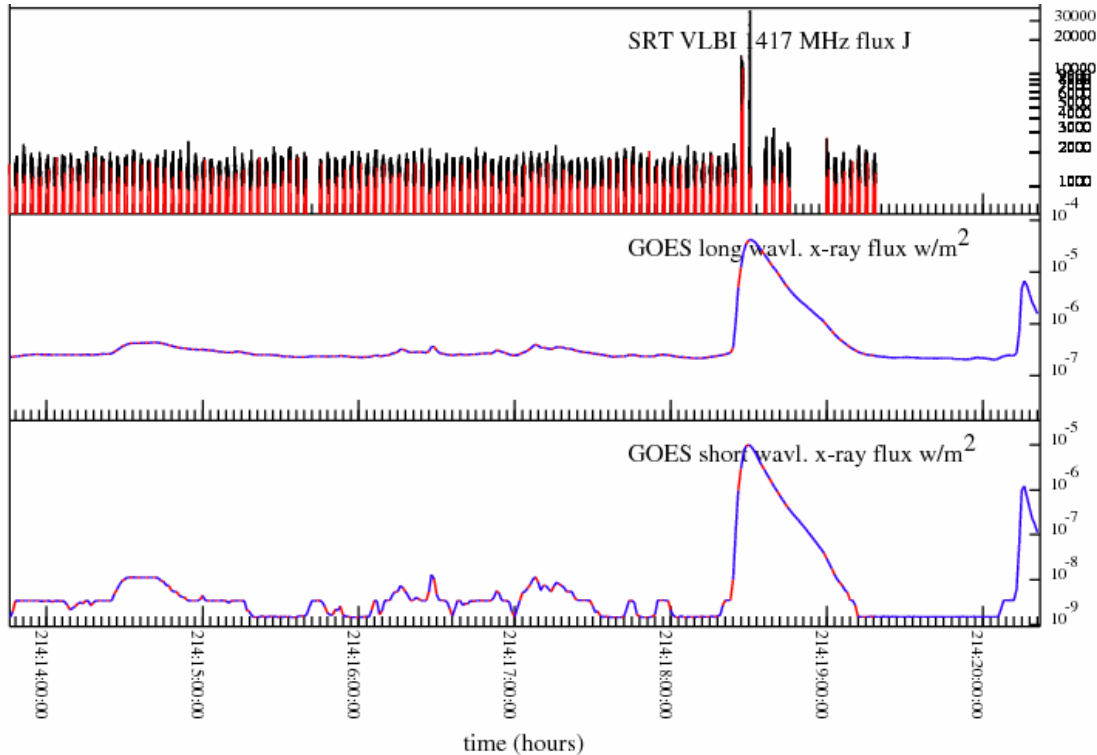
Figure 18 A several hour window around the burst recorded by the SRT interferometer on 2 Aug 2005 at 18:27 UT. This plot uses an integration time of 0.4096 seconds. The M-class solar flare shows up and immediately we see a burst in the SRT data.
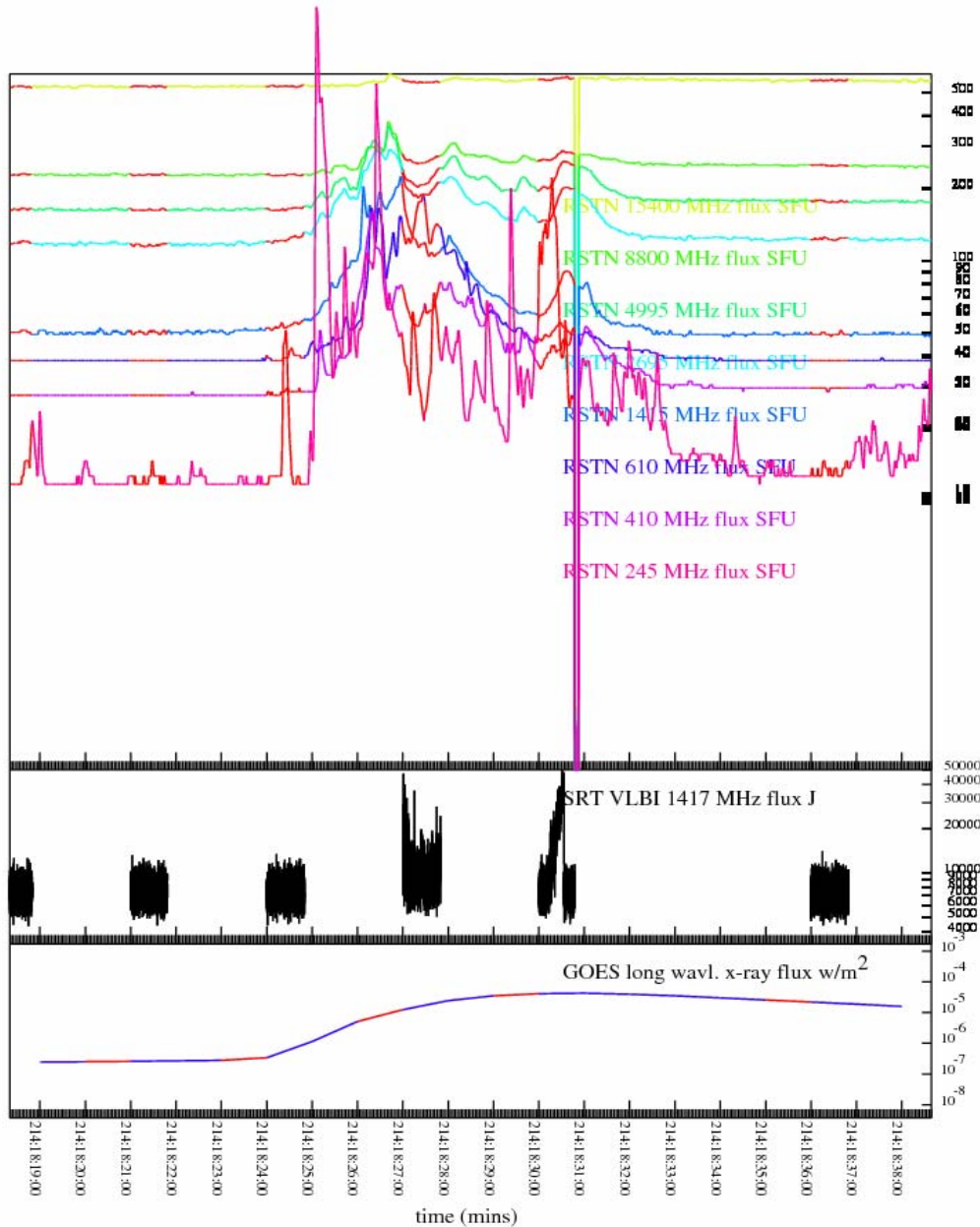
Figure 19 One of the early bursts observed in August 2005. In this plot, an integration time of 0.0128 seconds was used on the SRT data. This M-class solar flare is one of the first that suggested there might be a correlation between X-ray flares and the bursts observed by the SRT interferometer. In the more wide-ranged radio picture, this event seems associated with a lower frequency radio event that is moving towards the upper frequencies. By 15.4 GHz, barely any radio enhancement is observed. The vertical lines on the RSTN plot are artifacts of the plotting.

12 Sep 2005, 20:08 UT

This burst is associated with an M-class X-ray flare. As seen in the figure, this radio event is also seen in the higher frequencies up to 15.4 GHz and has no corresponding lower frequency components visible in the RSTN data. This burst is also a good example of the highly impulsive rise and the exponential decay typically observed with these types of burst.
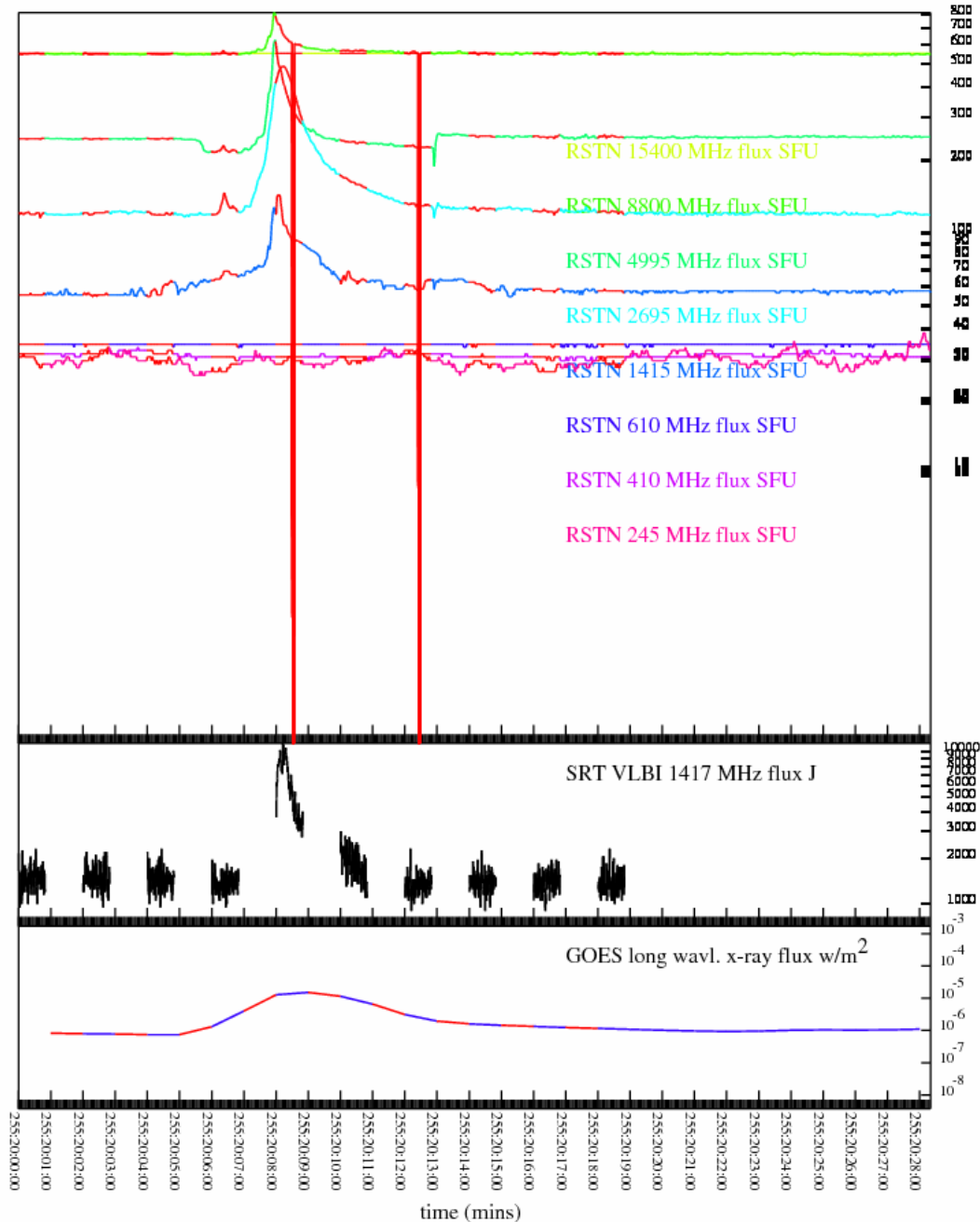
Figure 20 This burst occurred on 12 Sep 2005. This plot uses an integration time of 0.4096 seconds. The X-ray flare is an M-class flare. The radio activity seems to be all higher frequencies than 1415MHz for this flare. Upon close examination, the impulsive rise and exponential decay of the radio burst can be seen in the SRT data. Vertical lines in the RSTN plot are artifacts of plotting.

As I started looking at this event with shorter integration times, the burst does not permit other structure. On the contrary, the structure is preserved until it is lost in the noise at integration times shorter than 7.68 milliseconds.

Since the signal is no longer apparent to the naked eye on timescales shorter than 7.68 ms, I did not look at the spectrum of this burst.
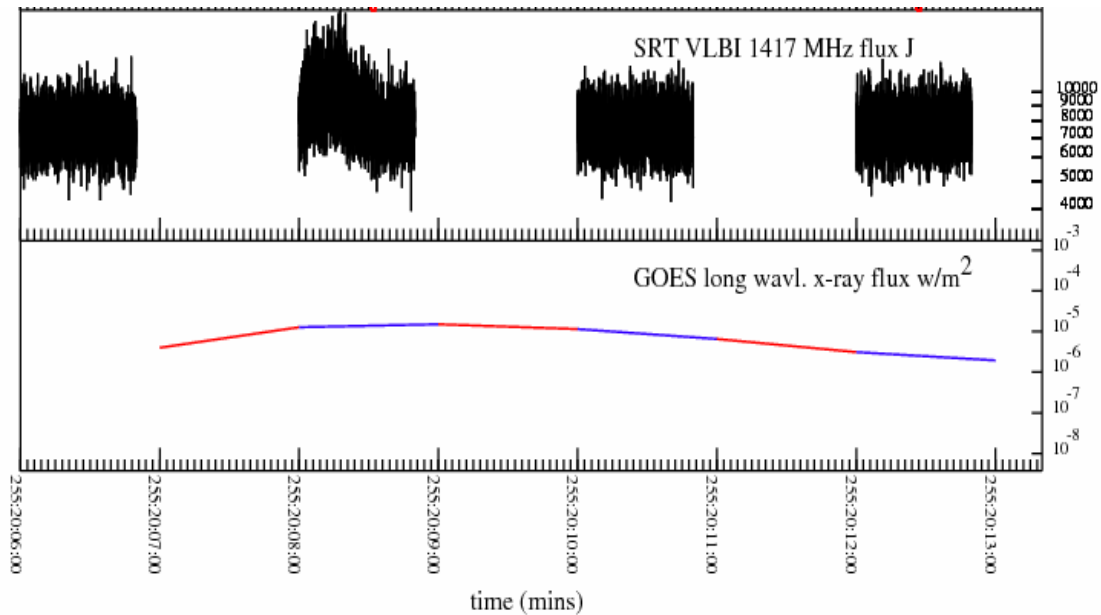
Figure 21 The same burst on 12 Sep 2005 with an integration time of 0.0128 seconds. The X-ray data is plotted for reference. This plot zooms to the area immediately around the burst. The rise time is not as evident in this plot as in the plot with the longer integration because of the wider noise variation at this timescale. The exponential decay can still be observed during the second SRT recording shown, which corresponds to the sharp rise and beginning of the decay in the previous figure.

13 Sep 2005, 19:24 UT

This group of bursts is by far the most interesting to study. For well over an hour, the SRT interferometer sees nearly continuous activity at levels far above the noise threshold.

At first glance, this X-ray flare is massive: it falls into the largest class of solar flares, X-class. Additionally, there appears to be 2 peaks only a few minutes apart, suggesting that this might be 2 distinct flares occurring nearly simultaneously. Right
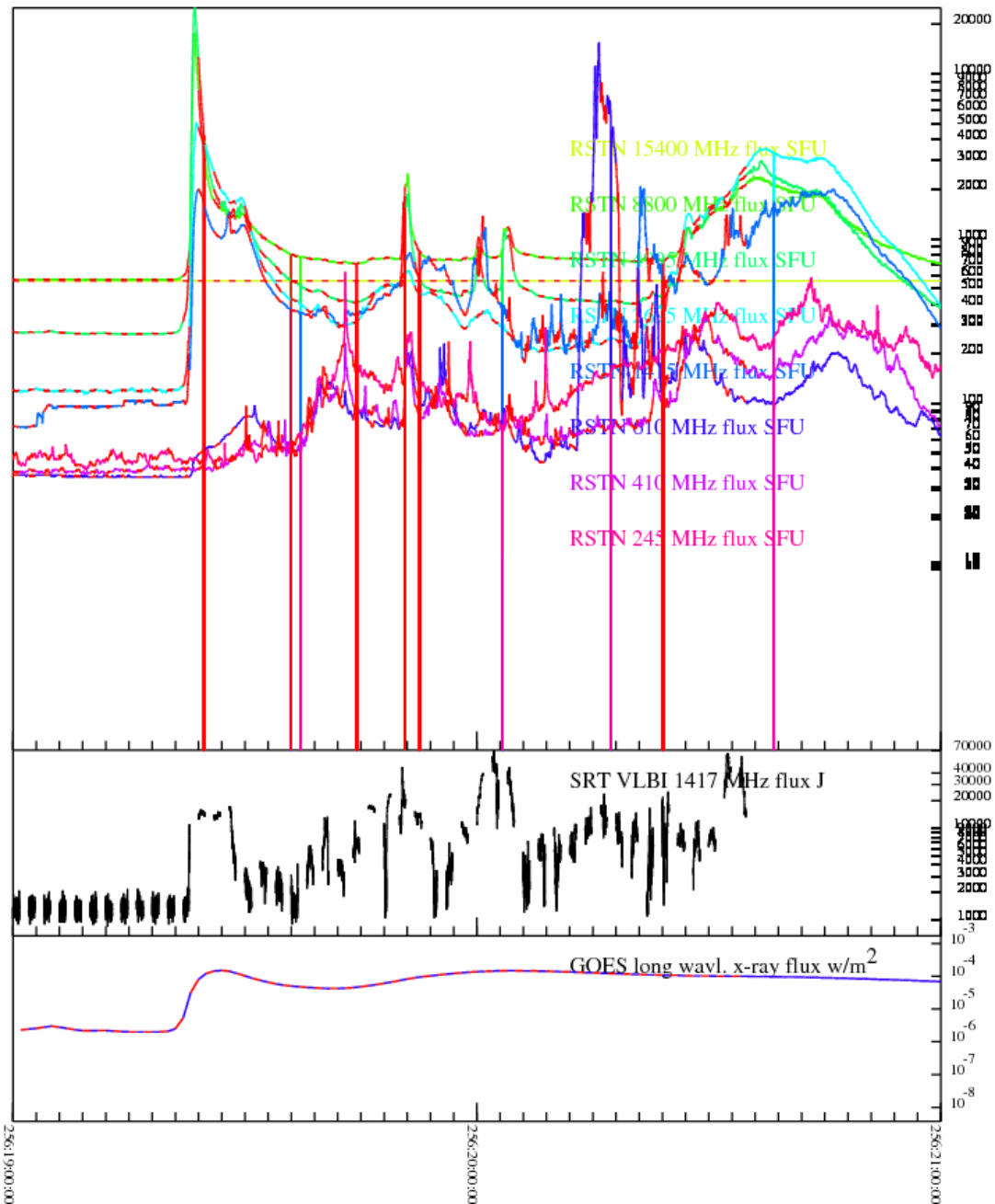
Figure 22 Bursts on 13 Sep 2005 with SRT integration of 0.4096 seconds. This X-class solar flare seems to have 2 peaks only tens of minutes apart. It is very possible that at different times during this period the SRT is seeing activity associated with different other frequencies. On the non-SRT plots, red line segments indicate that the SRT is recording. Vertical lines on the RSTN plot are artifacts of the plotting.

from the start, I am skeptical that we are seeing all of the structure in this set of bursts. Looking closely at the SRT data, many adjacent recordings show similar structures, such as both showing the rising edge of a burst or both covering the same flux levels with the falling edge of a burst. In a couple cases, adjacent recordings show the top of a burst: a rising edge, a peak, and a falling edge.

This radio activity is definitely associated with the X-ray burst, so next I looked at the RSTN radio data around this time. It is impossible to miss the sudden jump in solar activity at any of the frequencies recorded by RSTN at the start of this flare. The sudden impulsive rise seen in the SRT data matches quite well with the rise seen at 1415 MHz in the RSTN data. As we follow these two lines, however, they do not fit together as nicely. The best explanation I have for this discrepancy is the fact that the SRT interferometer resolves out the sun and simply looks at the bursting activity without the solar background. In this burst, it is obvious that the total radio flux of the sun at all frequencies increases for the duration of the X-ray flare. As such, the interferometer will only look at the variations around that total flux level. Additionally, the logarithmic scale used while plotting the SRT data will put extra emphasis on the smaller variations; however, the logarithmic scale cannot explain the significant rises seen by the interferometer when the RSTN 1415 MHz data show no peaks such as around 19:39 UT. It is possible that there is a peak in the RSTN data, but the increased total solar flux at 1415 MHz makes the peak more difficult to discern.

Continuing my study, I integrated the SRT data for shorter and shorting periods. The results are shown in the figures below.
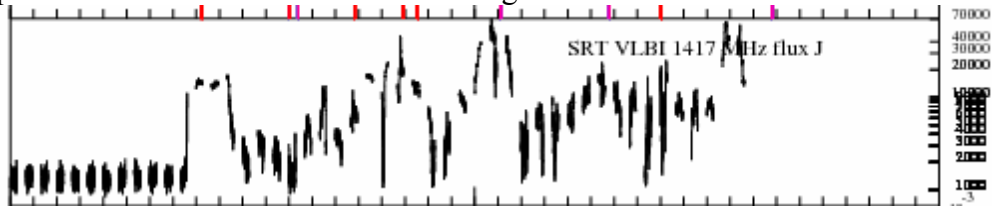
Figure 23 Integration time: 0.4096 seconds, Start 1900 UT, see Figure 31 caption
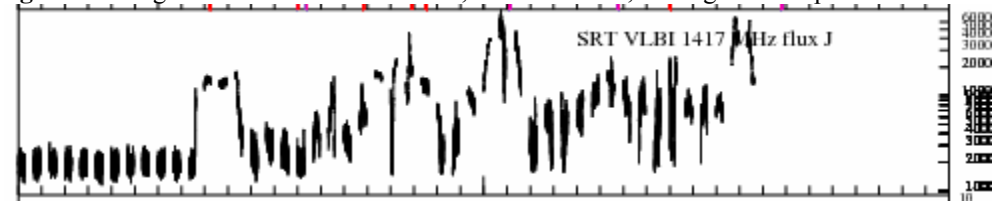
Figure 24 Integration time: 0.2048 seconds, Start 1900 UT, see Figure 31 caption
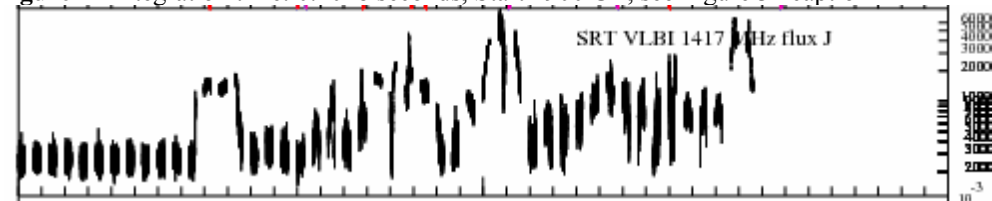
Figure 25 Integration time: 0.1024 seconds, Start 1900 UT, see Figure 31 caption

40
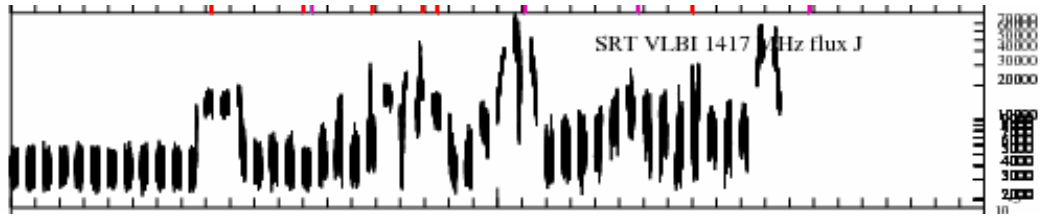
Figure 26 Integration time: 0.0512 seconds, Start 1900 UT, see Figure 31 caption
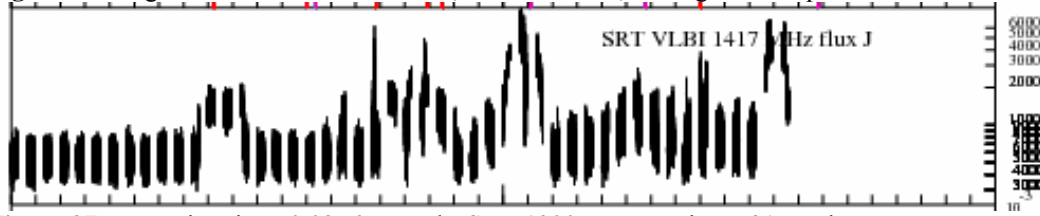
Figure 27 Integration time: 0.0256 seconds, Start 1900 UT, see Figure 31 caption
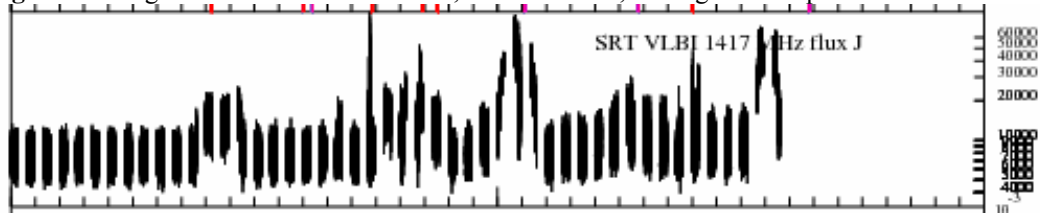
Figure 28 Integration time: 0.0128 seconds, Start 1900 UT, see Figure 31 caption
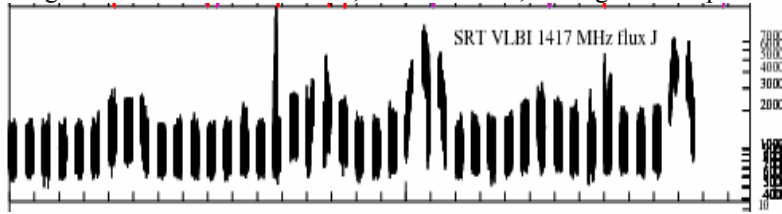

**Figure 29** Integration time: 0.00768 seconds, start 1912 UT, see Figure 31 caption
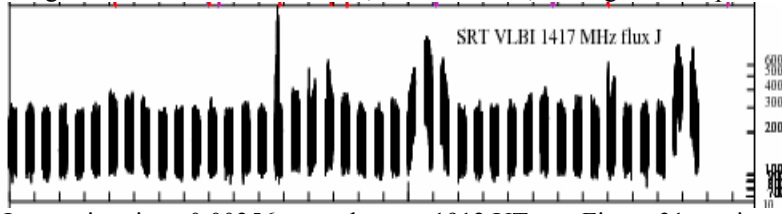
**Figure 30** Integration time: 0.00256 seconds, start 1912 UT, see Figure 31 caption
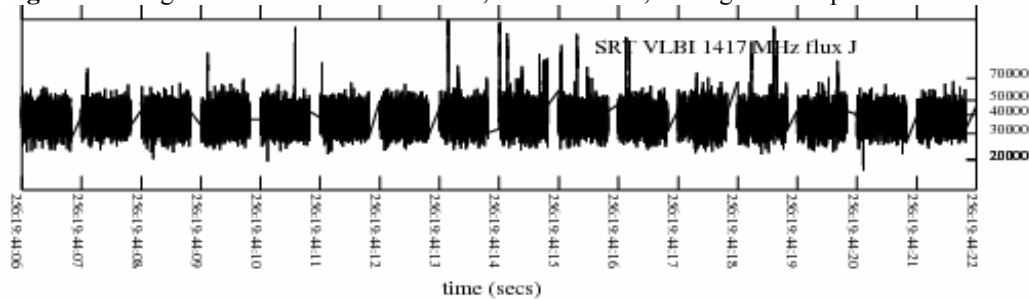
Figure 31 Integration time: 512 microseconds. This image zooms in on the single large peak still visible in the 0.00256 second integration. Working down from the 0.4096 integration, one can see that most of the peaks seen in the longest integration are simply absorbed into the noise as the integration time shortens. The peaks that sink into the noise do not have a shorter timescale structure. The peak that emerges at 19:44 UT indicates a signal that at the longer timescales is not very noticeable, but at the shorter timescales is very prominent. On all plots except the last, the times match vertically. Hash marks are placed every 3 minutes. The figures below zoom in on the various peaks in this image to see if these peaks are resolved or not.

41
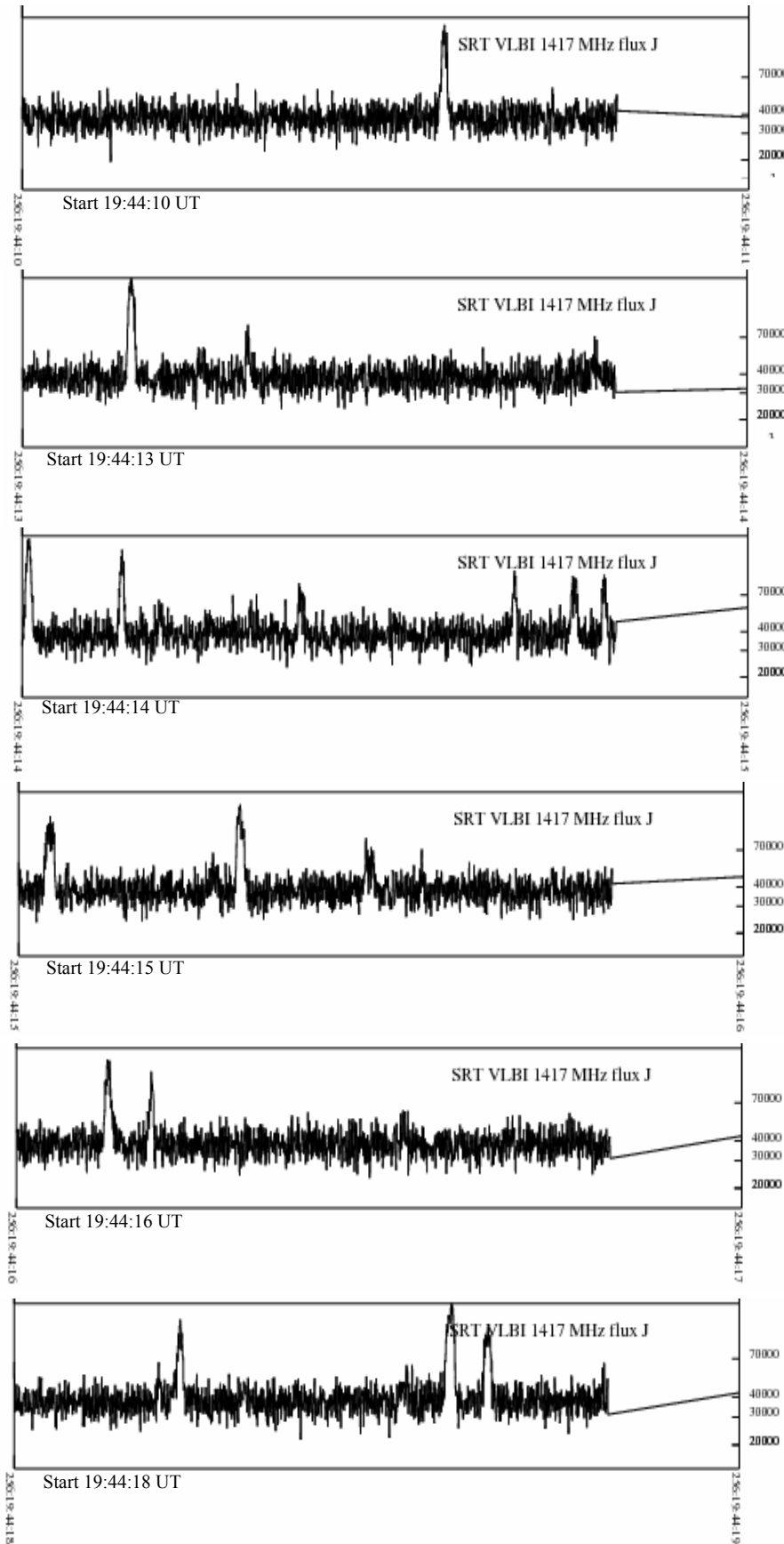
Figure 32 Data from SRT Interferometer using an integration time of 512 microseconds. In all of these images, the window covers a 1 second time slice of the data. The largest peaks in this dataset have a SNR of 13 or 14. All of these events are a few milliseconds long, and we have resolved all of them. At first glance, these bursts look like much shorter timescale versions of the larger and longer bursts we have seen to date.

42

As seen in the figures, most of the activity seen on 13 September 2005 does not have a finer structure than what is seen at the approximately half second integration level. There is, however, one spot of activity that is not very prominent at the half second integration level. This activity at 19:44 UT does not start to stand out until the integration time is down to 0.0256 seconds.

Upon closer examination of the peak at 19:44 UT, I discovered not one, but many distinct peaks. Personally, I was very surprised to see that the large peak at 19:44 UT contained many individual spikes. I had not previously given serious consideration to activity on this timescale from the sun.

Next, I proceeded to look at the spectrum of each of these events seen in the 1 second blowups on the previous page (Figure 32). Within each of these spectra, a similar pattern is observed consisting of a set of peaks that drifts in frequency over time.
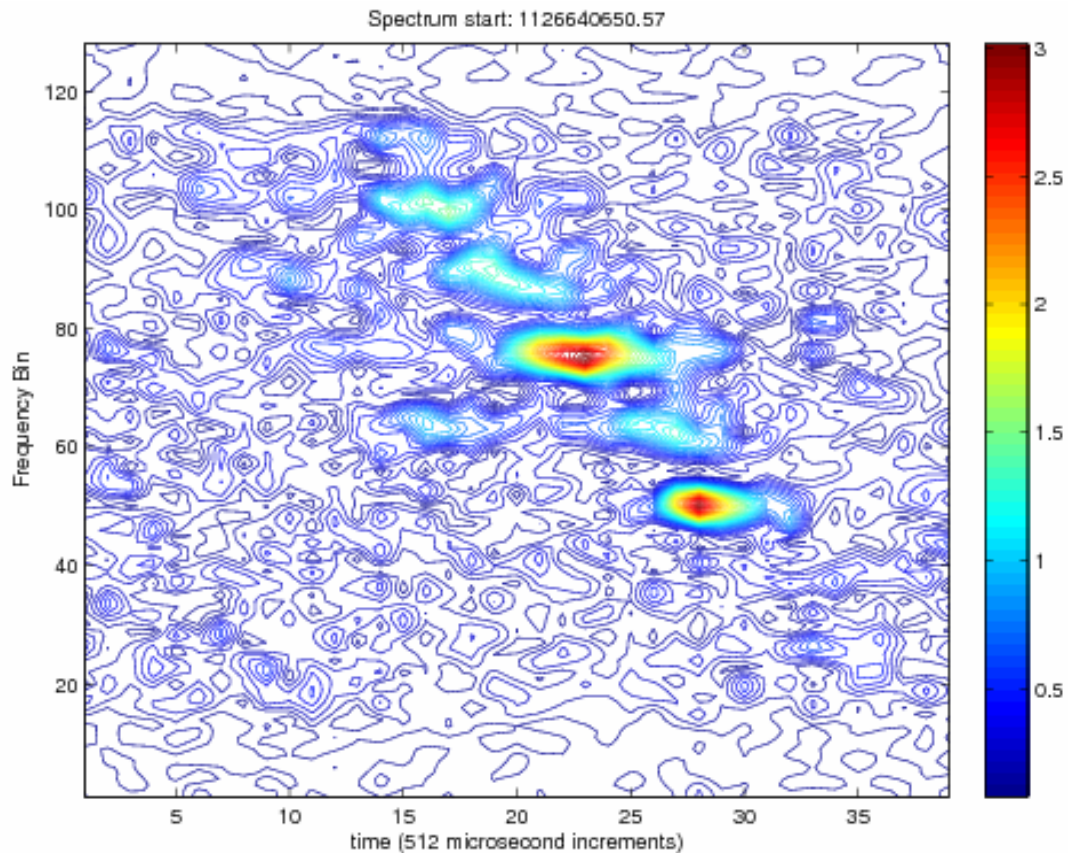

Figure 33 Burst 19:44:10.57 Frequency increases with bin number, 31.25KHz per bin. Drift Rate - 281.4 MHz/s, Average Frequency separation between peaks 399.2 KHz. This burst shows simple structure with 2 strong peaks.
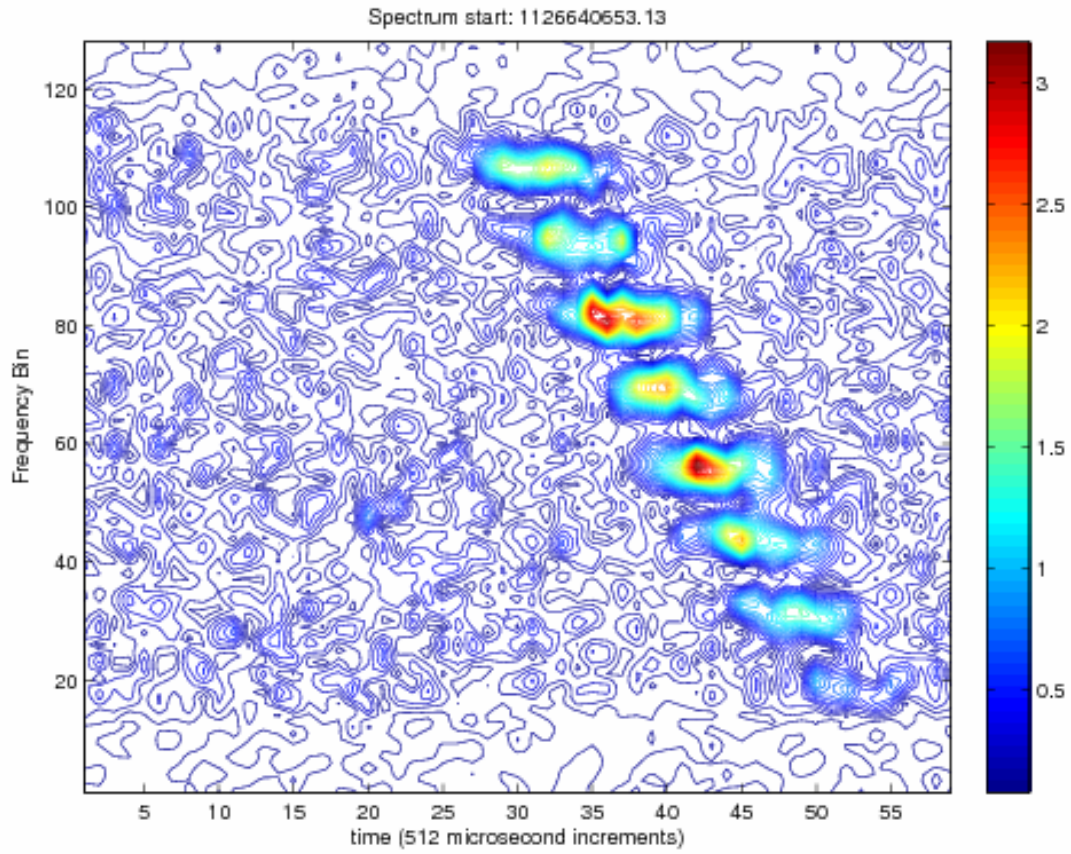
Figure 34 Burst 19:44:13.13 Frequency increases with bin number, 31.25KHz per bin. Drift Rate -270.9 MHz/s, Average Frequency separation between peaks 389.4 KHz. Some peaks in this burst show a distinct double peak. We have no explanation for this double peak at this time.
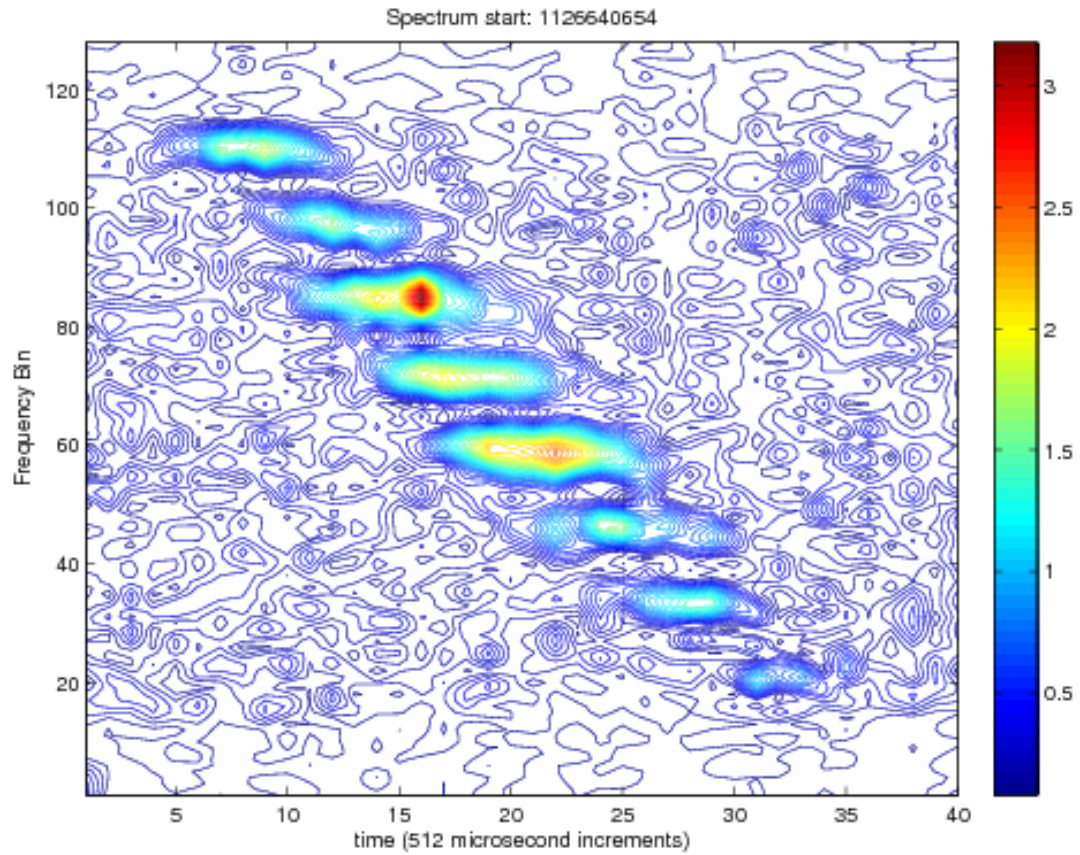
Figure 35 Burst 19:44:14.00 Frequency increases with bin number, 31.25KHz per bin. Drift Rate -245.7 MHz/s, Average Frequency separation between peaks 400.9 KHz. Again a fairly simple structure, but looking closely one can see a slight downward drift within a single peak.

Spectrum start: 1126640654.13
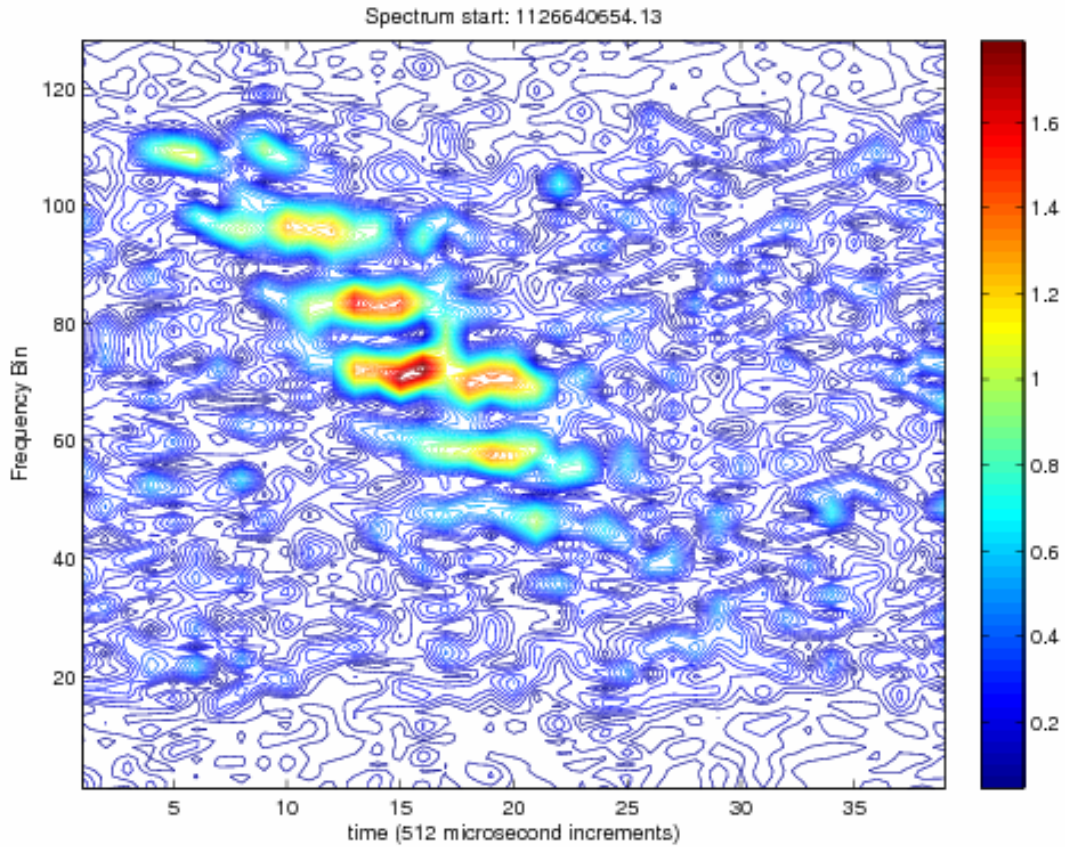
Figure 36 Burst 19:44:14.13 Frequency increases with bin number, 31.25KHz per bin. Drift Rate -298.2 MHz/s, Average Frequency separation between peaks 396.8 KHz. This burst exhibits slightly more structure within the peaks than the previous bursts. It is possible this structure is more evident because of the weaker maximum of this burst.

Spectrum start: 1126640655.03
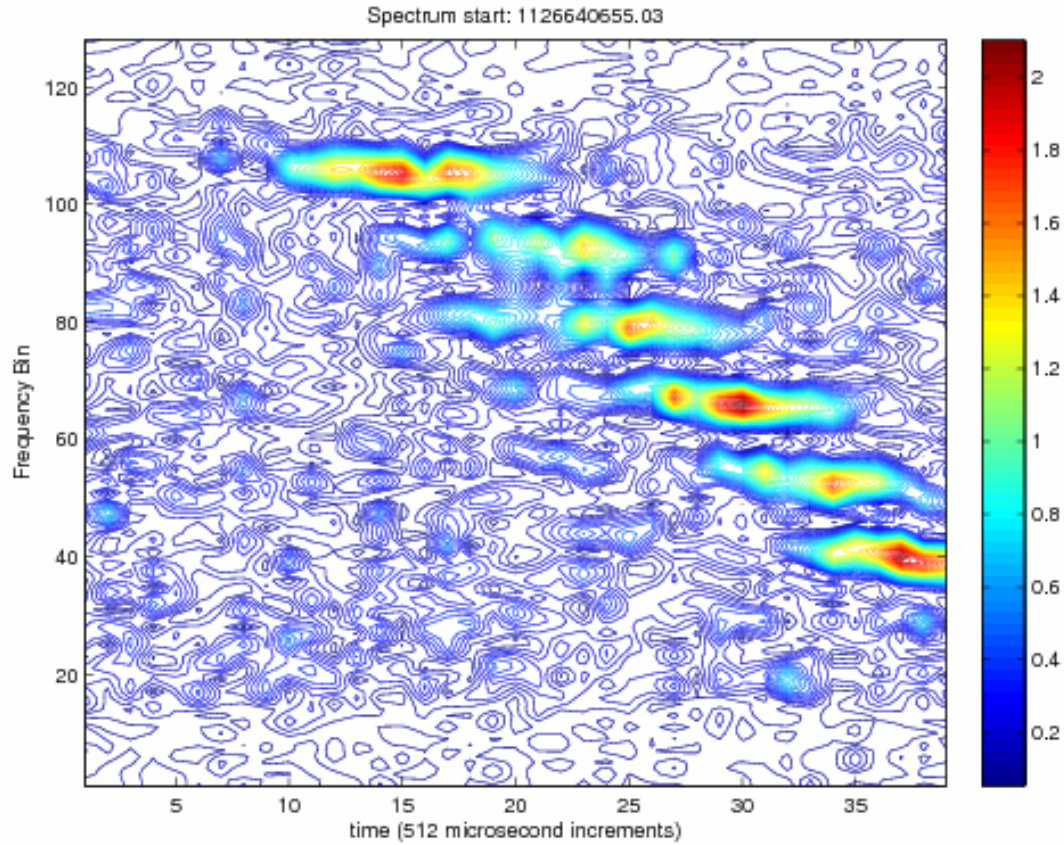
Figure 37 Burst 19:44:15.03 Frequency increases with bin number, 31.25KHz per bin. Drift Rate - 223.7 MHz/s, Average Frequency separation between peaks 400 KHz. Again, a lot of internal structure is observed. We have no clear explanation for this structure
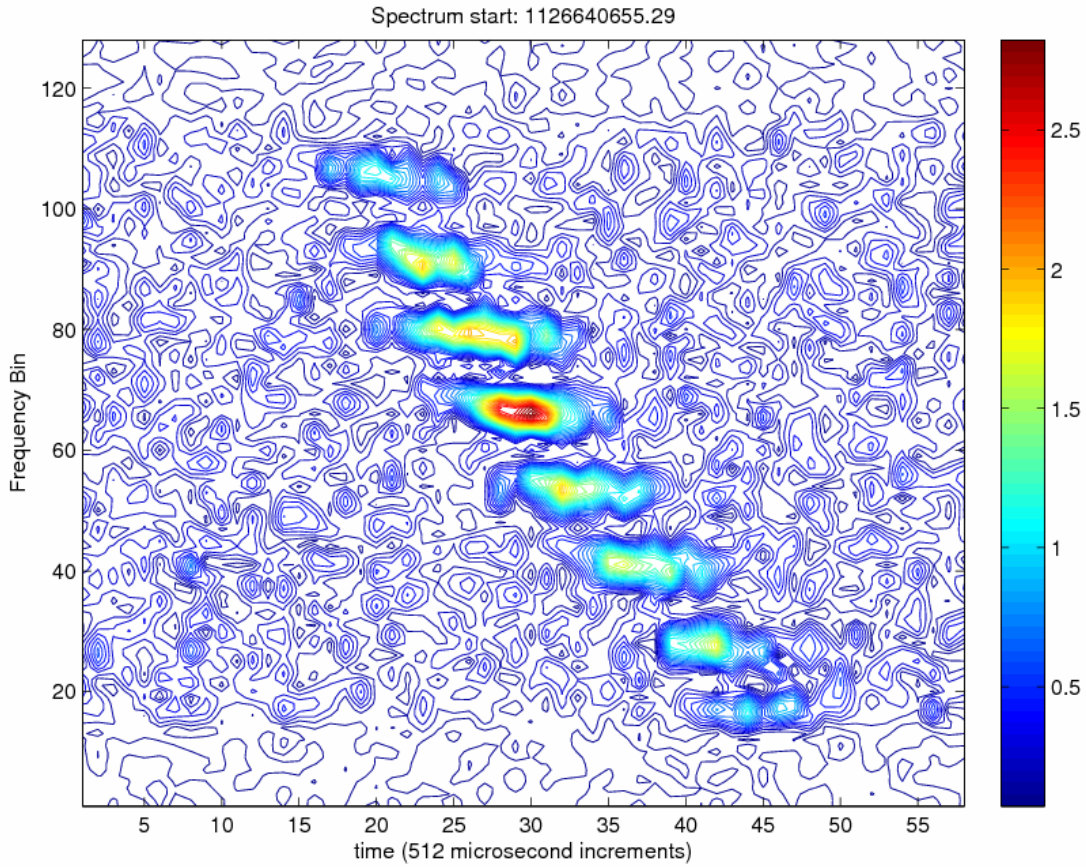
Figure 38 Burst 19:44:15.29 Frequency increases with bin number, 31.25KHz per bin. Drift Rate - 219.2 MHz/s, Average Frequency separation between peaks 400.9 KHz. Looking closely, this burst deviates from a linear frequency drift. Additionally, each internal burst shows drifting.

Spectrum start: 1126640656.11
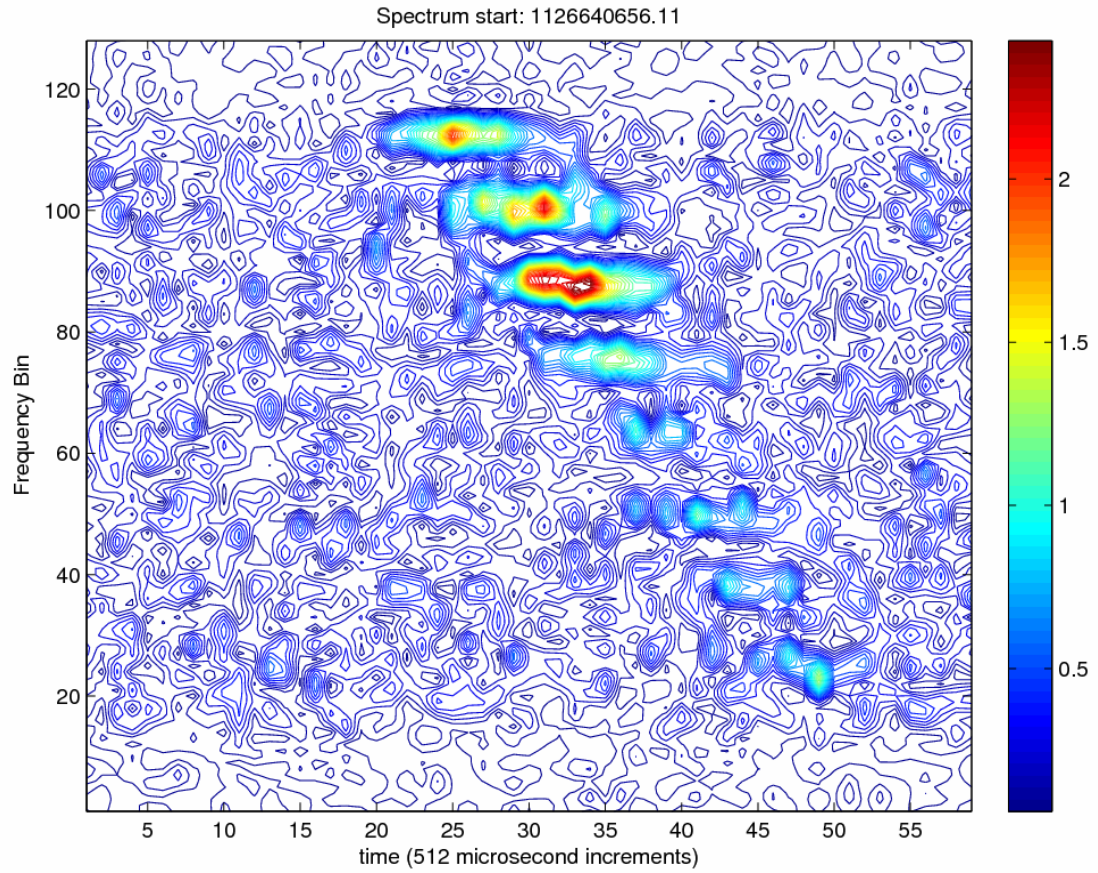
Figure 39 Burst 19:44:16.11 Frequency increases with bin number, 31.25KHz per bin. Drift Rate - 248.86 MHz/s, Average Frequency separation between peaks 400.9 KHz. Some unusual structure is present including several peaks in each burst.
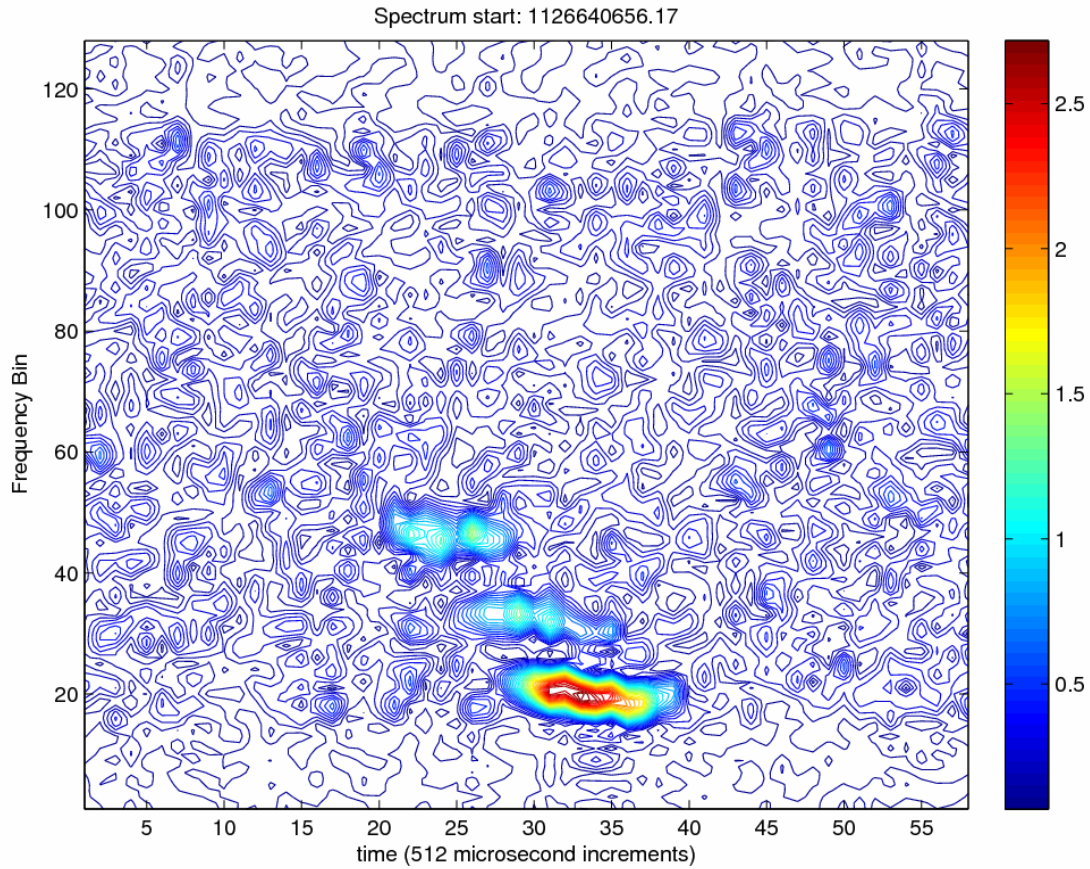
Figure 40 Burst 19:44:16.17 Frequency increases with bin number, 31.25KHz per bin. Drift Rate -172.2 MHz/s, Average Frequency separation between peaks 427.4 KHz. This burst appears to start within our bandwidth and quickly drift out of the band.

50
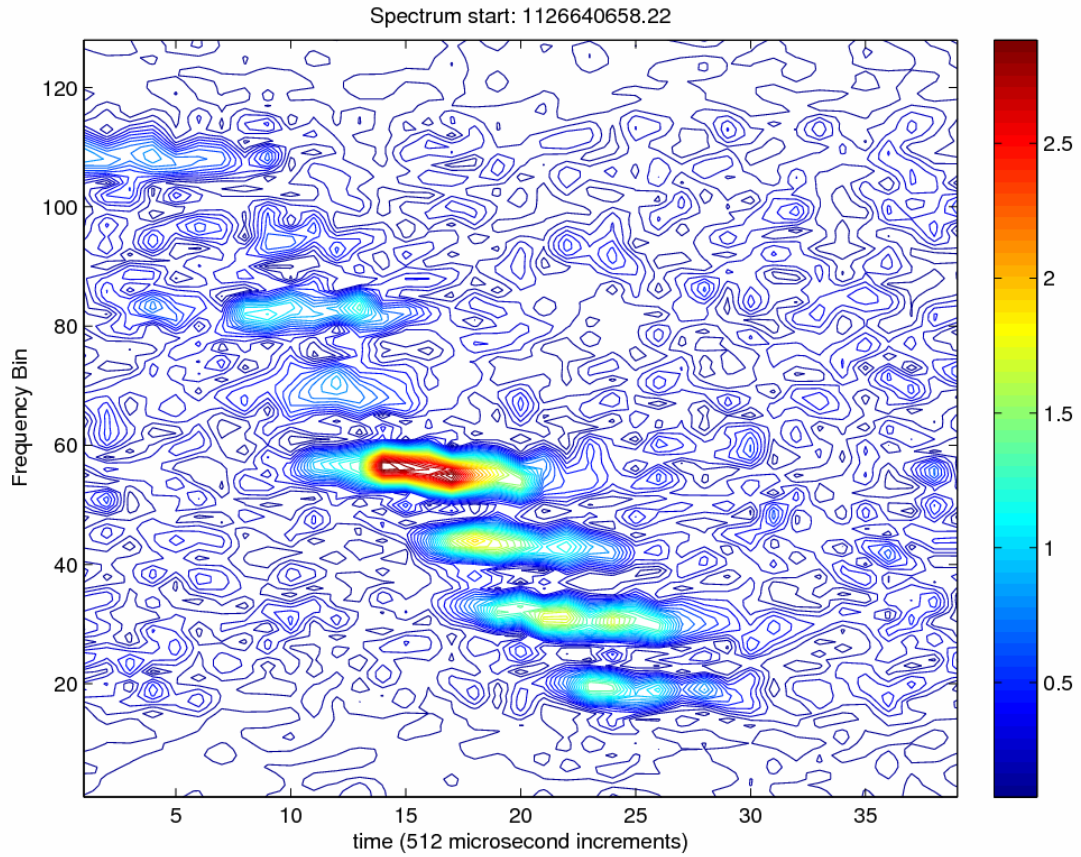
Figure 41 Burst 19:44:18.22 Frequency increases with bin number, 31.25KHz per bin. Drift Rate - 255.2 MHz/s, Average Frequency separation between peaks 393.5 KHz. This burst shows long individual bursts with possibly two peaks.
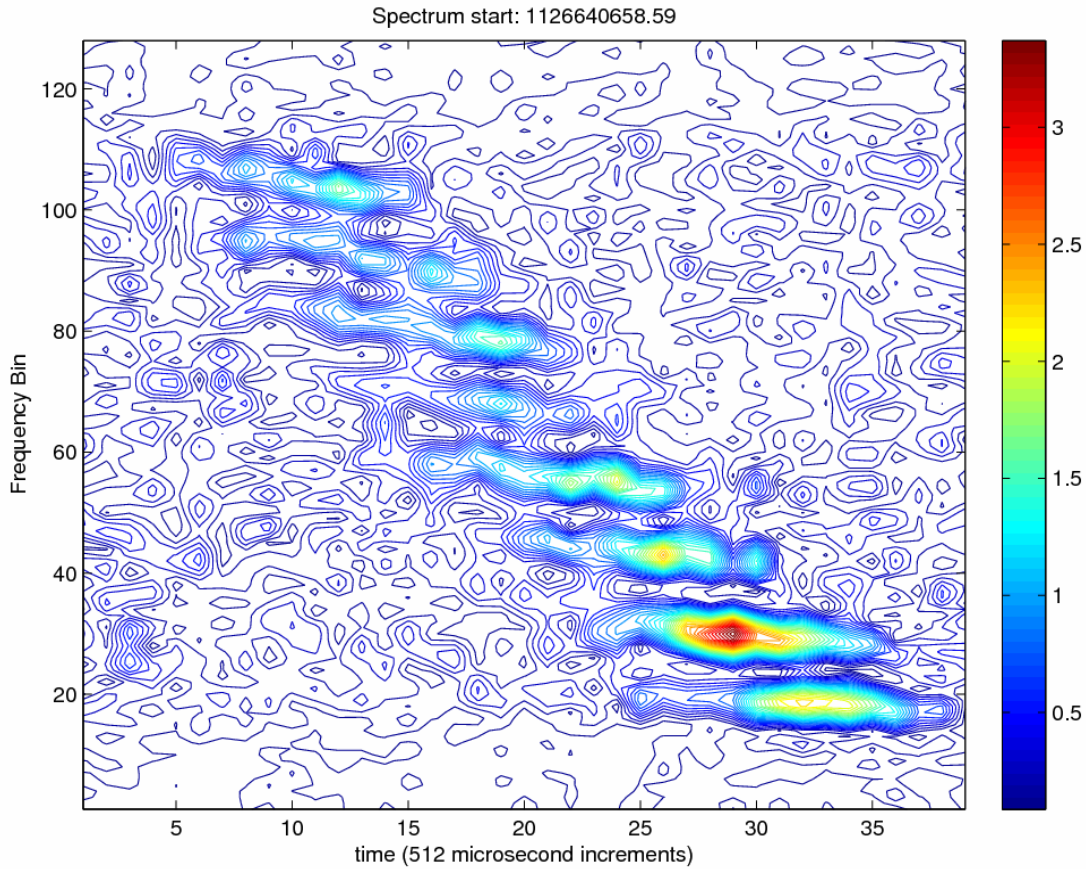
Figure 42 Burst 19:44:18.59 Frequency increases with bin number, 31.25KHz per bin. Drift Rate -264.6 MHz/s, Average Frequency separation between peaks 387.1 KHz. This burst starts rather weak at the top with lots of internal drift, but becomes more stable with less drift internally at the bottom.
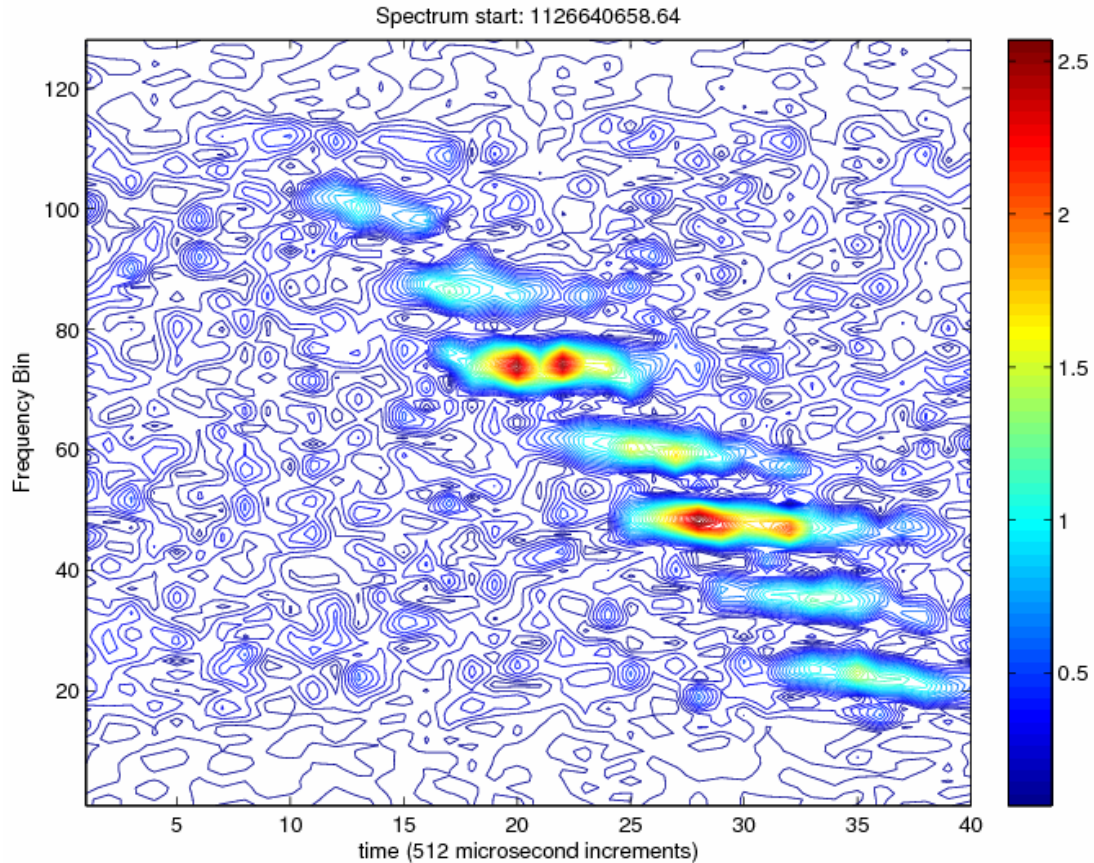
Figure 43 Burst 19:44:18.64 Frequency increases with bin number, 31.25KHz per bin. Drift Rate -198.5 MHz/s, Average Frequency separation between peaks 403.2 KHz. Several very close strong peaks are evident in this burst.

One of the most surprising things from a first look at these plots is the defined peaks and valleys. After eliminating any possibility of instrumental error, plotting artifacts, or miscalculations, we are confident that this is a real phenomenon. To the best of our knowledge, no one has observed this type of activity at this frequency band. The only connection we have seen is a group of papers written in the early 1980's that saw something similar at low frequencies of 20-100 MHz. We do not know if there is any connection between these low frequency observations and our observations. The statistics recorded about these low frequency bursts are very different than ours, but after adjusting for some type of frequency dependence it is possible that the statistics could be similar.

Table 3

Start Time on 13 Sep 2005	Slope (MHz/sec)	Average spacing between peaks (Khz)
19:44:10.57	281.4	399.2
19:44:13.13	270.9	389.4
19:44:14.00	245.7	400.9
19:44:14.13	298.2	396.8
19:44:15.03	223.7	400.0
19:44:15.29	219.2	400.9
19:44:16.11	248.8	400.9
19:44:16.17	172.2	427.4
19:44:18.22	255.2	393.5
19:44:18.59	264.6	387.1
19:44:18.64	198.5	403.2

With these 11 bursts there are some statistics that describe the phenomena that we see. The drift rates range from 172.2 MHz/sec to 298.2 MHz/sec. The frequency space between individual peaks ranges from 322 KHz to 419 KHz. See Table 3 for detailed information. The next thought becomes "is there a pattern?" To look for a pattern, I plotted each pair of data from Table 3. In some cases, it looks like a pattern could exist, but in other cases, adjacent bursts that are less than a tenth of a second apart have vastly different statistics. Possibly, each pattern that emerges belongs to a different location on the sun. If we believe all of the current theories about solar phenomena, all activity is caused directly or indirectly by solar magnetic fields. As such, different points on the sun have sometimes vastly different magnetic fields. A very different magnetic field will produce phenomena with very different characteristics.
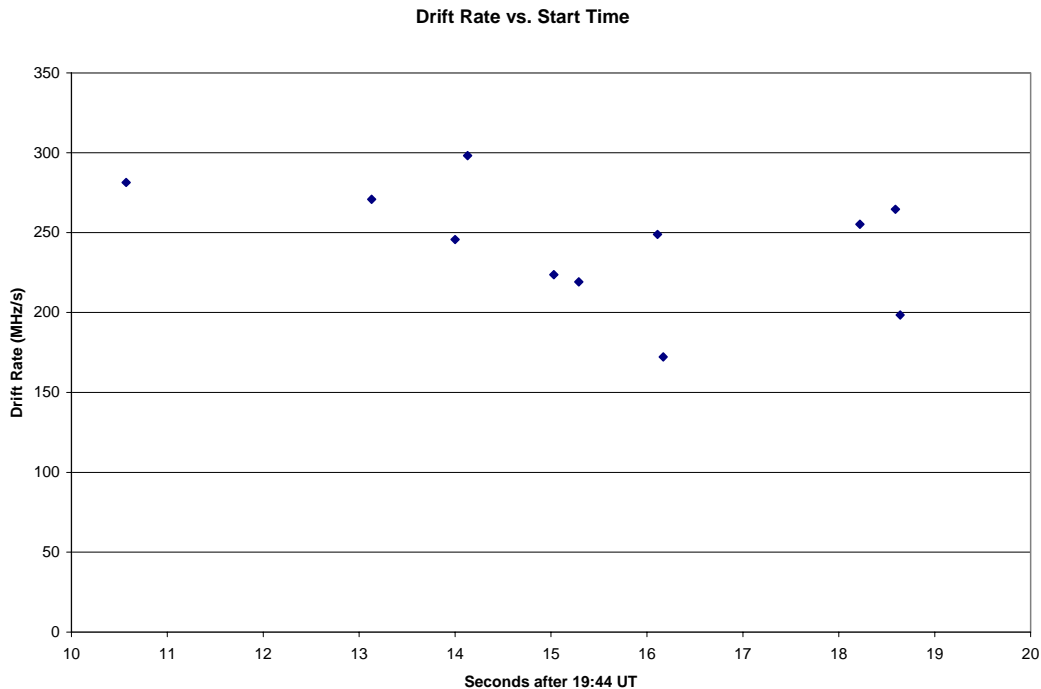
**Figure 44** Data from drifting bursts seen with digital spectroscopy.

Average spacing between peaks (Khz) vs. Start time
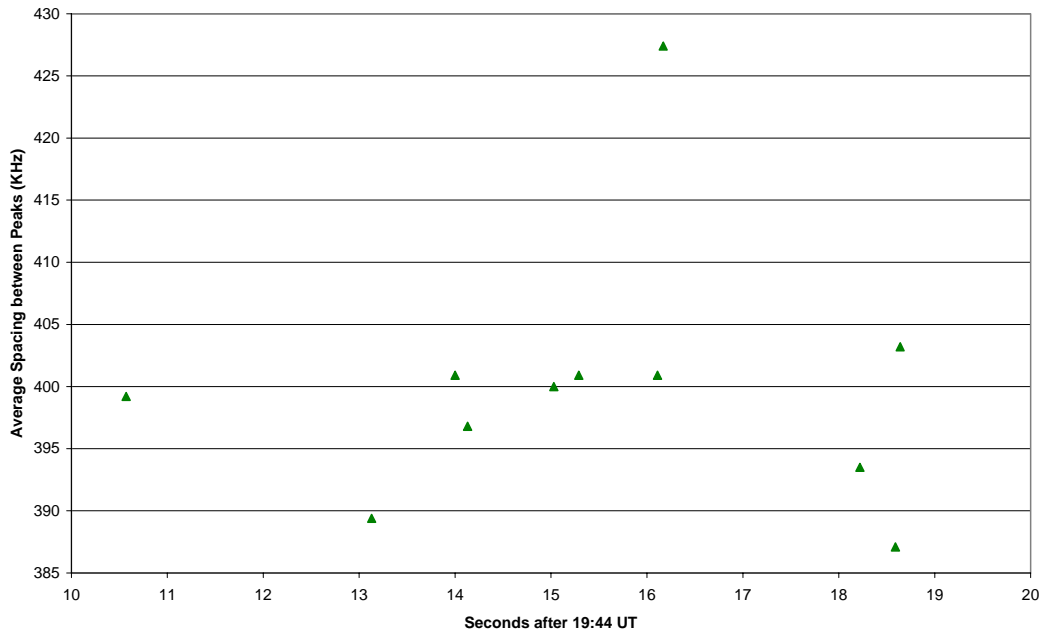
Average spacing between peaks (Khz) vs. Drift Rate (MHz/s)
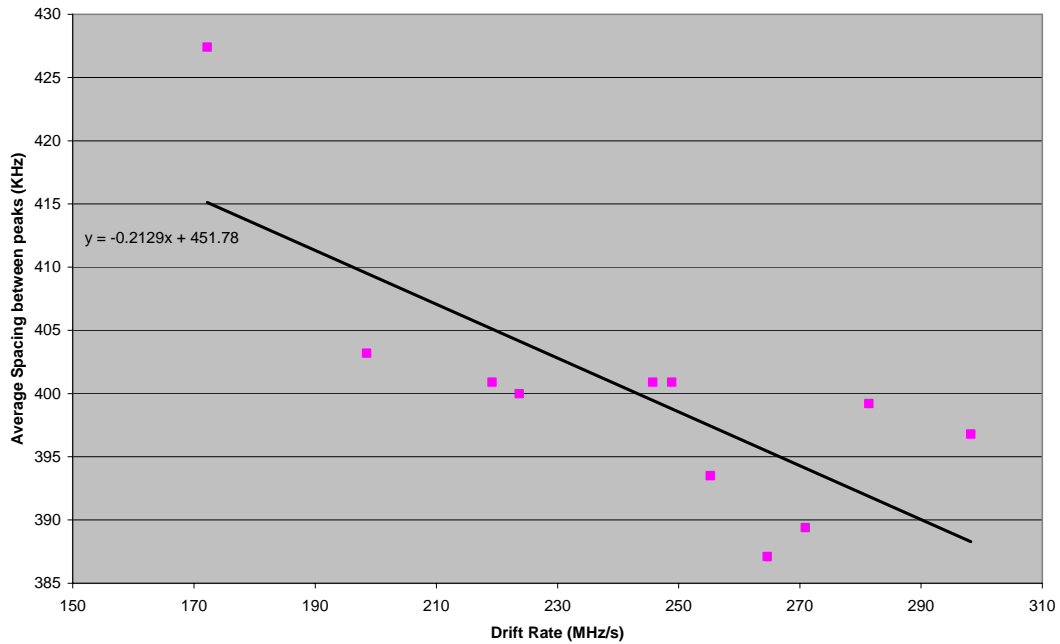
Figure 45 Data from drifting bursts seen with digital spectroscopy. For the final plot of Average spacing vs. Drift rate, the correlation coefficient is -0.758

In each of the previous plots referring to drift rate, two somewhat linear trends seem apparent. The spacing between peaks, however, appears to be nearly random. I do not yet know how to interpret these findings in terms of a physical system, but it is possible that these data produce some insight.

15 Sep 2005, 19:00 UT

This burst is only seen in a single SRT recording, but it is corroborated by the occurrence of an X-ray flare and a higher frequency set of peaks on the RSTN plots. No fine structure emerges upon probing at shorter integration times. No other plots are included because we only saved the single recording containing the burst activity due to hard drive constraints faced during our recording days. The plotting software did not like to plot that single recording properly, but it did plot enough for me to be confident that no smaller structure exists.
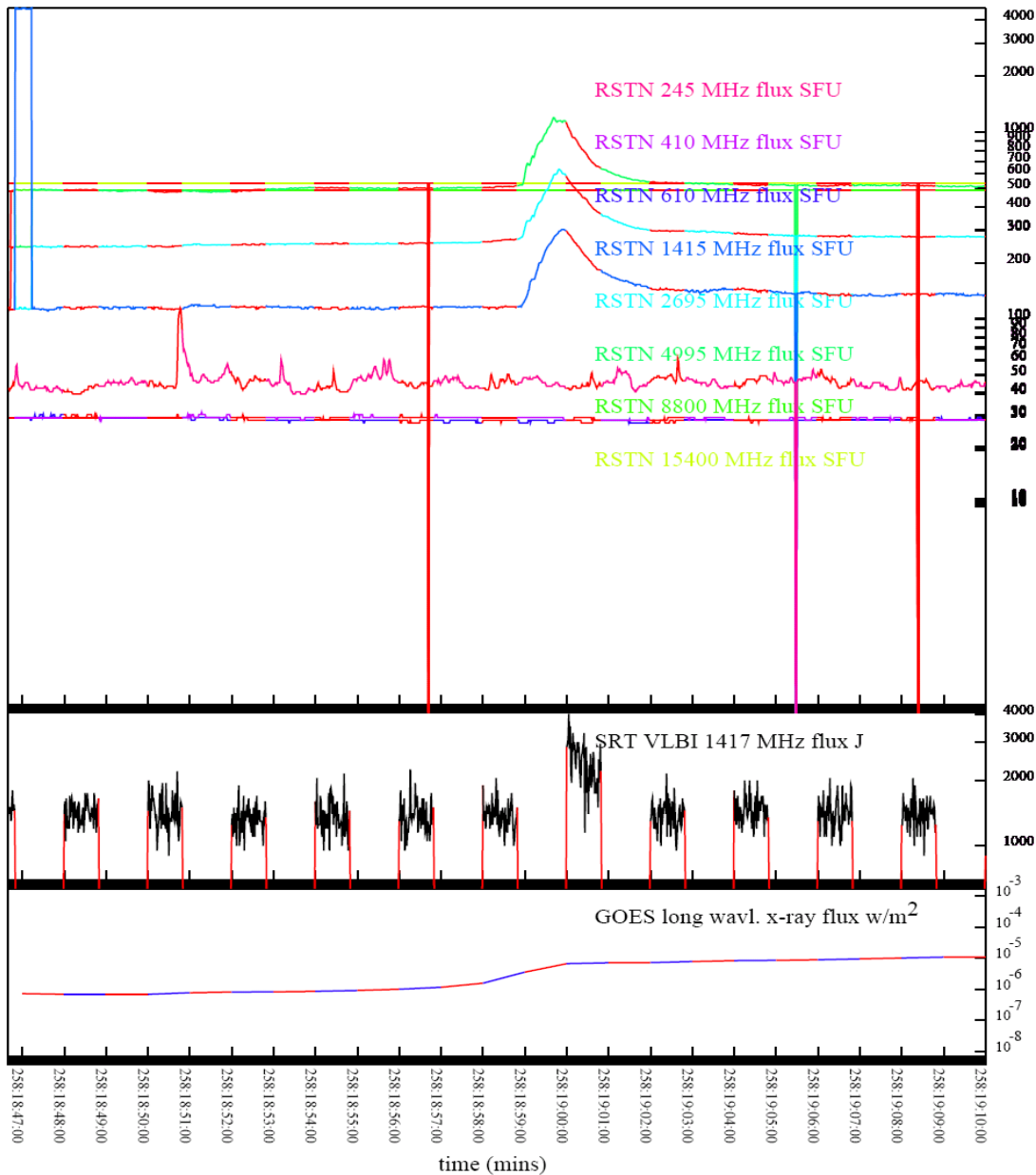
Figure 46 Burst at 19:00 UT 15 Sep 2005. Integration time 0.4096 seconds. The SRT data matches quite well with the 1415 MHz RSTN data. The burst occurs at the rising edge/peak of the large C-class X-ray flare. The amplitude of this burst is far smaller than the amplitude of the SRT bursts associated with M-class or X-class solar flares. The radio activity seems to be associated with higher frequency radio signals. Vertical lines on the RSTN plots are plotting artifacts.

56

16 Sep 2005, 17:44 UT

The first of two groups of bursts on 16 Sep, this is another somewhat weak burst with a maximum at less than 10,000 Janskys. The flare associated with this burst is an M-class flare, but only just barely. There does not appear to be any significant burst activity in any of the radio frequencies monitored by RSTN at the time we observe our burst. There do appear to be a couple of small bumps in the RSTN 1415 MHz data that are in the right places to be associated with our burst and also have the correct approximate magnitudes. At shorter integration times, these bursts disappear into the rising noise which suggests no internal structure.
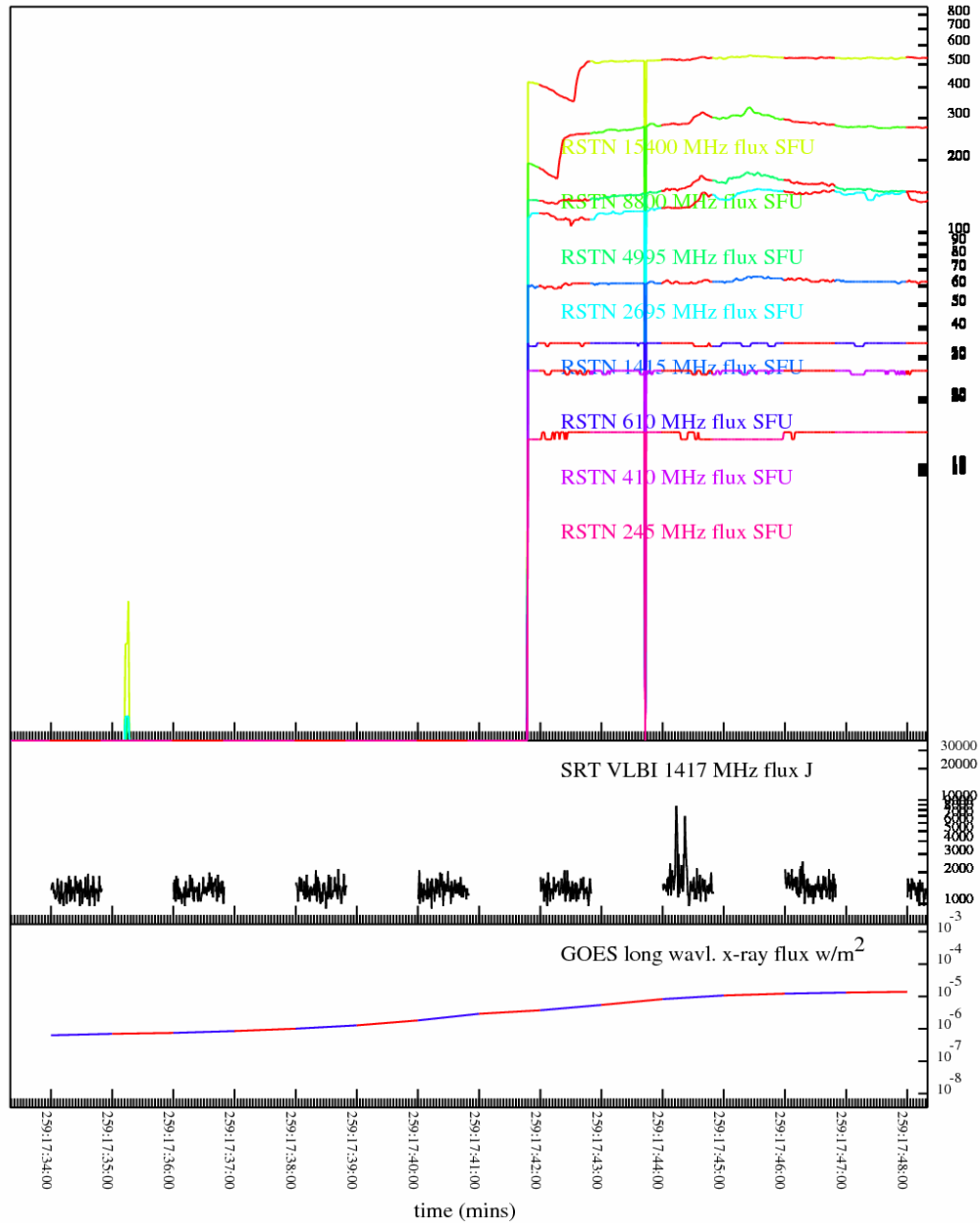

Figure 47 Two skinny bursts at 17:44 UT on 16 Sep 2005. For most of this window, no RSTN data are available, but data exist for the time of the SRT burst. Looking very closely at the 1415 MHz RSTN data, there are two tiny bumps at the right times to match up with the two bumps seen on the SRT recording. The SRT fringe amplitude is approximately 1 SFU (10,000 Jy = 1 SFU), so the tiny bumps on the RSTN data are approximately the correct size, just much more difficult to see. The burst occurs along the rising edge of an M-class X-ray flare

16 Sep 2005, 19:30 UT

The second of two bursts on 16 Sep, this burst group proves interesting to study. At first glance, two things jump out: this is an M-class solar flare and there is strange structure in the high frequency RSTN data. The other precarious feature is the short 20 SFU spike seen in the RSTN 1415 MHz data around 19:30 UT. This spike is not as surprising when taken in light of a similar but smaller flux spike seen in the SRT data.
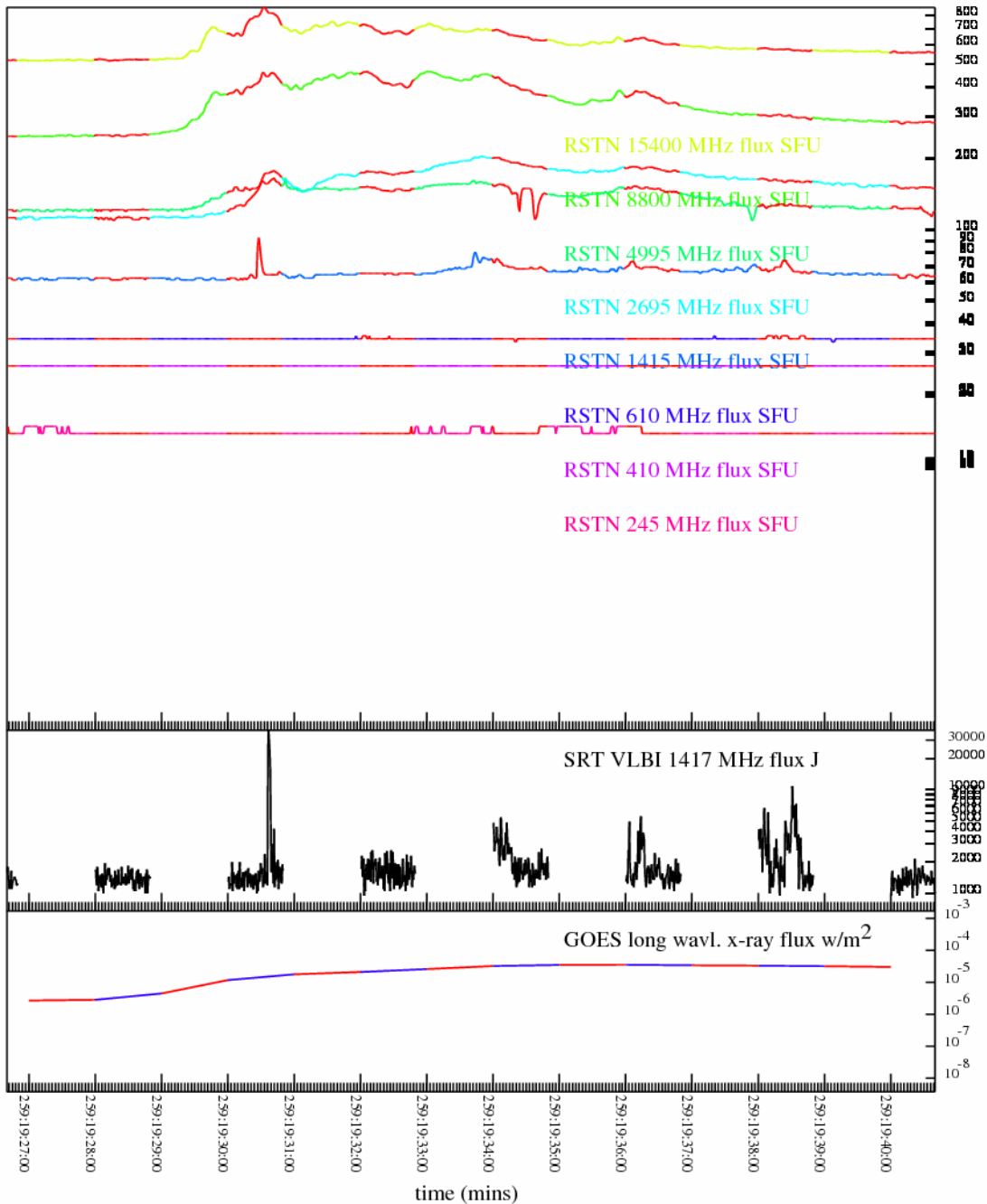

Figure 48 Several interesting bursts starting at 19:30 UT on 16 Sep 2005. The first activity is seen along the rising edge of this M-class solar flare. At a 0.4096 integration time, the SRT data shows similar structure to the 1415 MHz RSTN data. RSTN data show an unusual high frequency structure that is not visible in any other major burst.
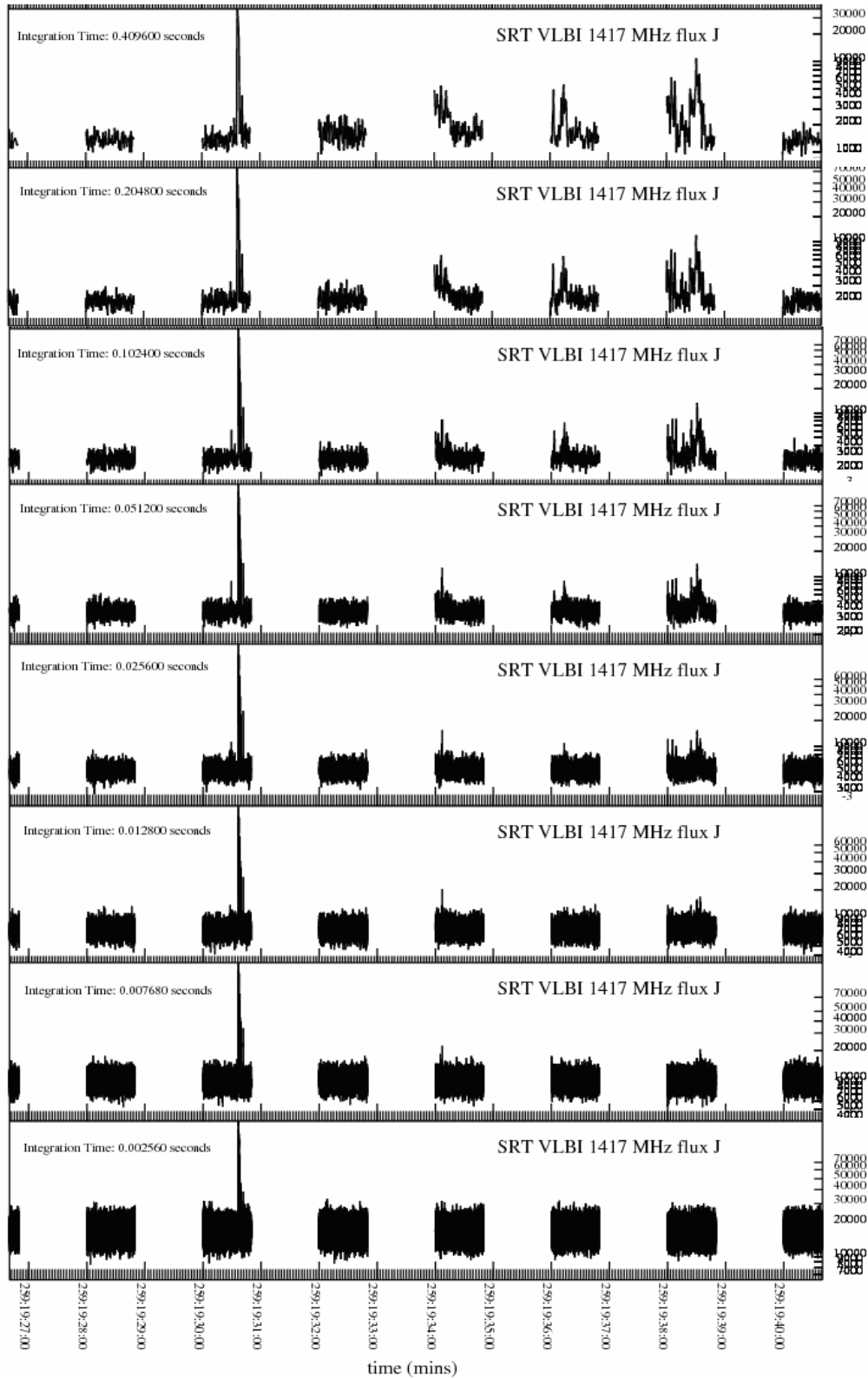
Figure 49 Burst 16 Sep 2005 at 19:30 UT. Integration time decreases towards the bottom of the page. Only the peak in the recording at 19:30 remains visible at the shortest integrations. Looking very carefully, at 0.4096 sec integration, this peak looks like a single rise and fall with white space underneath the curve. At shorter integration times, the lack of white between the rise and fall suggest several independent events.
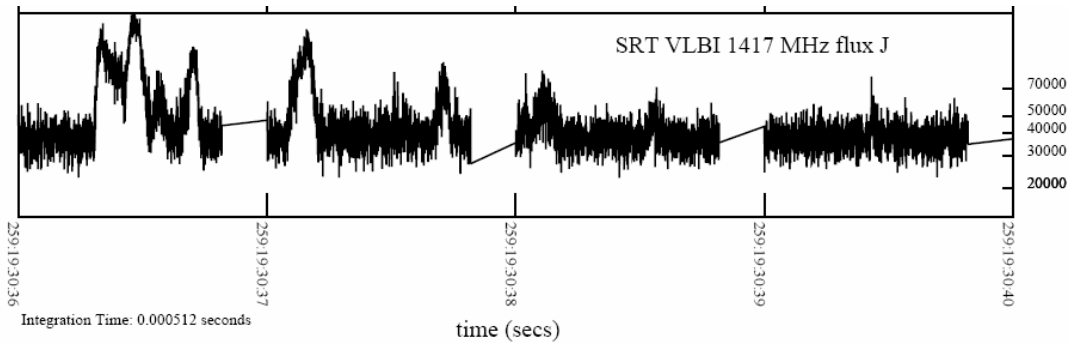
Figure 50 Magnification of the large peak at 19:30 UT on 16 Sep 2005 using an integration time of 512 microseconds. These bursts look similar to the bursts seen on 13 Sep 2005, but each burst here lasts for longer than any of the bursts seen on 13 Sep. Also, the bursts here are not as well defined as the bursts seen previously. Lines connecting each recording block are artifacts of the plotting. There is a short gap between one second recordings.

After the initial observations, the time arrives to look at shorter integrations. Upon examination of these shorter integrations, a group of about 7 bursts is observed over the span of 4 seconds. These bursts at first look are similar to the 13 Sep bursts, but of a much longer duration. Being of a similar structure, it makes sense to look at the spectrum of these bursts to see if they are actually the same distinctive pattern as seen previously.
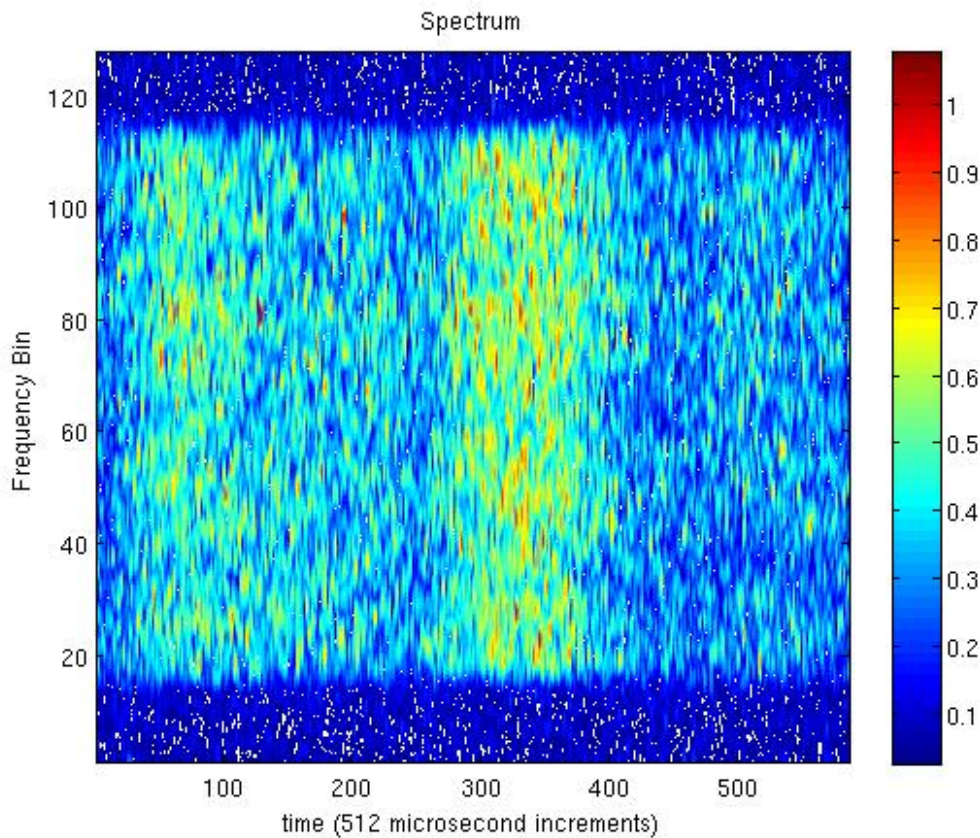

Figure 51 Burst starting at 19:30:36.3 on 16 Sep 2005. As previously, frequency increases with bin number, 31.25KHz per bin. This plot shows the first two peaks shown in Figure 50. The maximum peak intensity here is approximately 1/3 of the peak intensity seen in most of the compact drifting bursts on 13 Sep 2005.

60

As seen in Figure 51, these bursts exhibit a distinct band of enhanced flux. Also, these bursts have maximum flux values that are about 1/3 of the maximum flux observed during the bursts on 13 Sep, although the flux integrated across the bandwidth still reaches similar values to the 13 Sep bursts. At this point it is difficult to know for sure if this burst activity is caused by the same mechanism as the previously observed bursts. My first reaction is to believe that this activity is caused by a different mechanism, but since neither mechanism is known, no proof can be presented here.
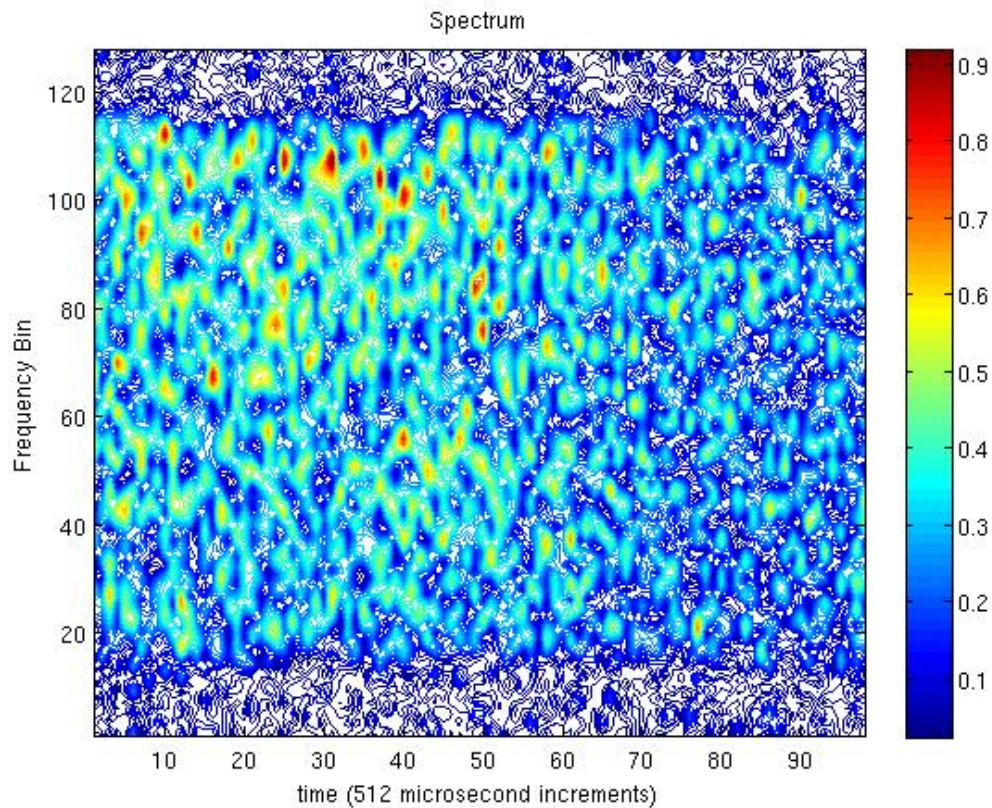

Figure 52 Burst starting 19:30:36.69, 31.25KHz per frequency bin. While no obvious structure is present, the general decrease in flux from the top of the bandwidth to the bottom in the left half of this plot indicates that some kind of activity is occurring.
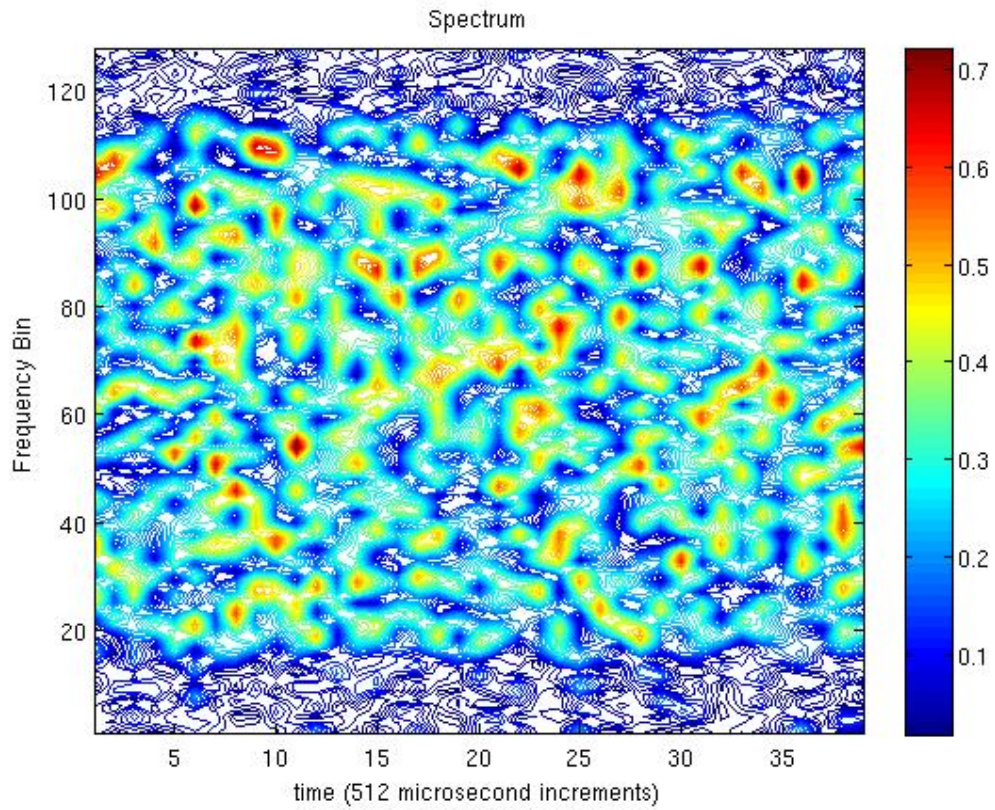
Figure 53 Burst starting 19:30:37.10, 31.25KHz per frequency bin. This burst has a smaller max flux than most of the plotted bursts in this group. Lots of high points with nearby lows are visible, but no obvious structure jumps out.
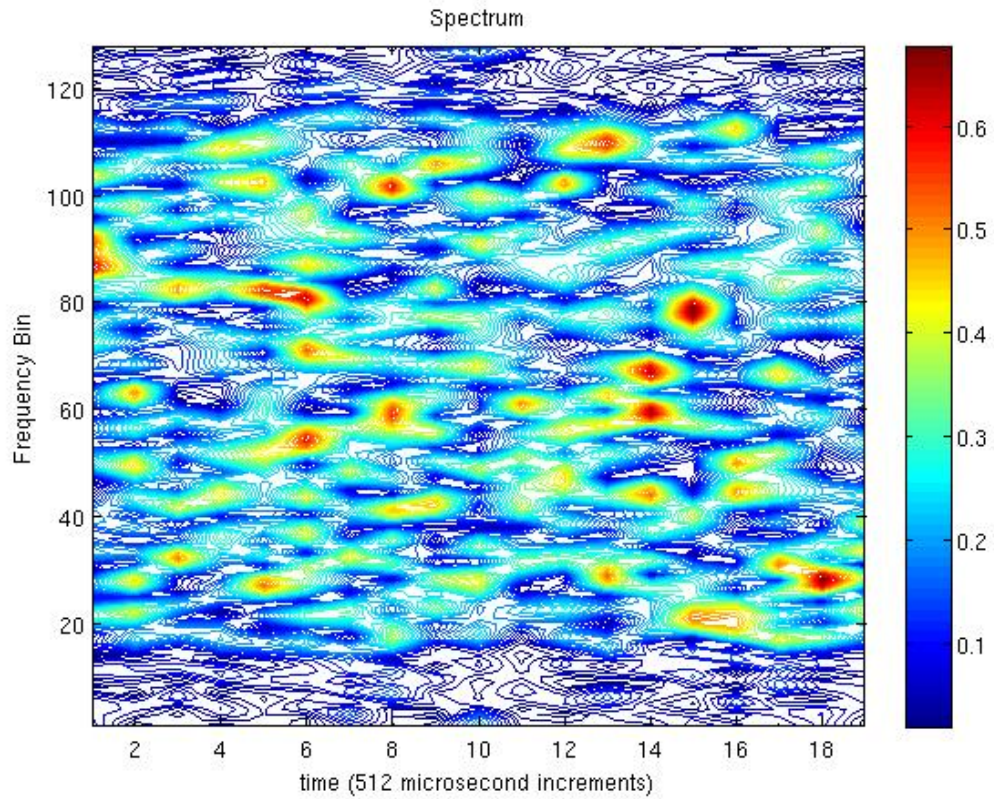
Figure 54 Burst starting 19:30:37.25, 31.25KHz per frequency bin. The weakest burst plotted from this group, nothing particularly exciting seems to be happening here. Most of the structure less than 0.5 is simply noise that is not so visible in other plots because of the color scale when the highest point in higher.
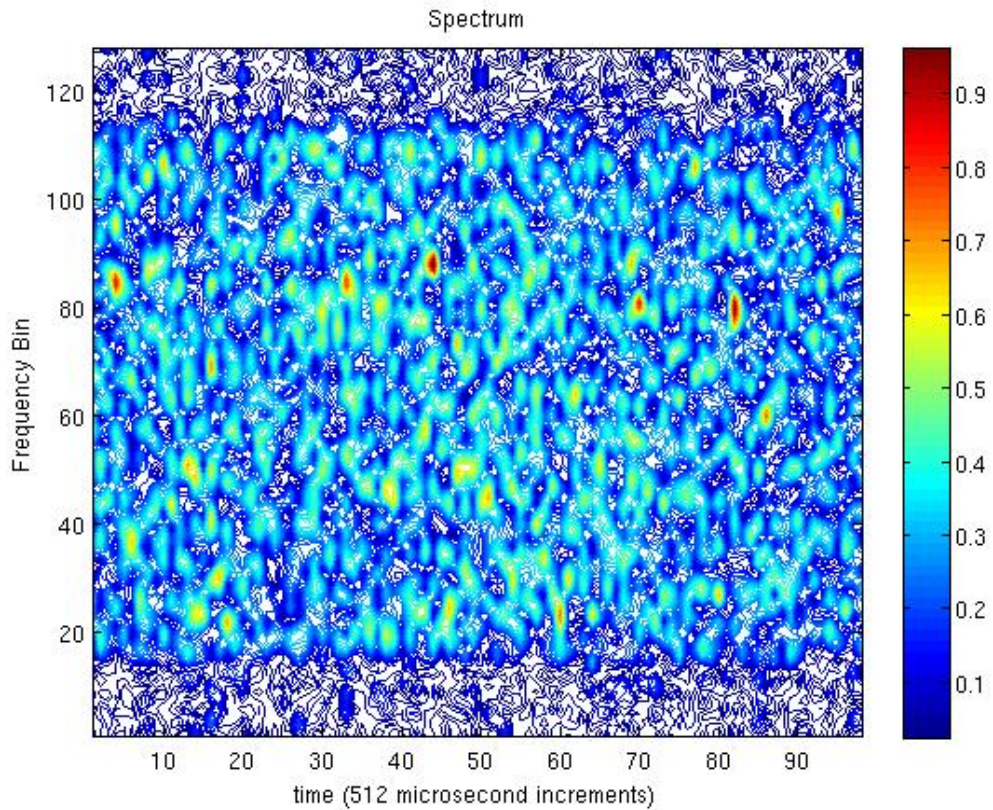
Figure 55 Burst starting 19:30:37.69, 31.25KHz per frequency bin. Unlike the other bursts in this group, this burst has very distinct peaks in very compact frequency-time space. This structure suggests that there might be something very interesting occurring to cause this phenomenon.

18 Sep 2005, 19:32 UT

   The last burst large enough to talk about here, this burst started at 19:32 UT on 18 Sep 2005. Characteristics recorded by the SRT interferometer are very similar to the 12 Sep 2005 burst studied earlier.   At a B-class level of X-ray activity, the sun is not very active at any frequency when this burst is observed; however, a radio enhancement is observed in the 1415 MHz RSTN data at the same time as the SRT burst.
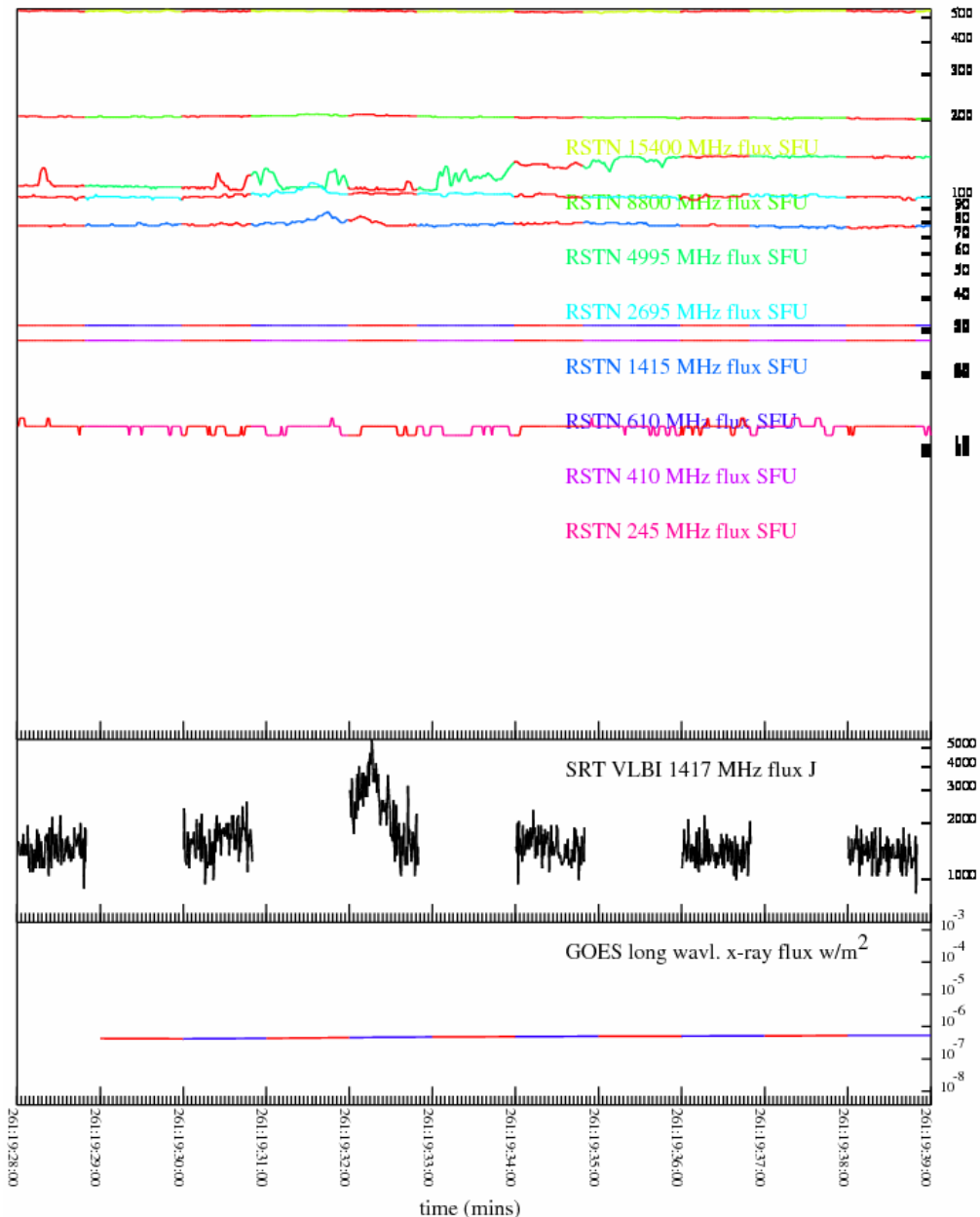

Figure 56 Burst starting at 19:32 UT on 18 Sep 2005. X-ray levels would be classified as B-class. This burst has similar SRT characteristics to the burst on 12 Sep 2005. This particular plot shows 0.4096 second integration time. With an SNR of about 3, this burst definitely happened, but is not large enough to warrant significant study at this time. In all bands of the RSTN data, the sun is not highly active. The spot where we see a burst in SRT does correspond to a time showing enhanced emission at 1415 MHz in the RSTN data.

Conclusions

We used the Haystack Observatory Small Radio Telescope Interferometer to observe the sun. Most of the time, no strong fringes are observed. At most once or twice in an observing day, strong fringes are seen that correspond to other activity in radio and X-ray frequencies as seen by RSTN and GOES respectively.

We have determined that this is an appropriate instrument to use while looking at the sun, particularly at areas the size of an active region on the sun. This interferometer will reject the background solar radiation and show a strong signal only if there is a burst or flare of some type above the solar background. This instrument is very sensitive and will detect even a small burst with a reasonable signal to noise ratio.

At the end of this research, while we know far more than we did at the beginning, a lot of questions still remain.

I have determined that for every M-class or larger solar flare that occurs while the SRT interferometer is recording, a burst of some type is recorded by the SRT interferometer. At other flare levels, we do occasionally see an SRT burst, but not always. At this point, there may or may not be a connection between maximum X-ray flux and maximum SRT burst flux.

After a closer look, this study of the sun proceeded to examine the sun at higher frequency resolution than any other previous solar study. As we look at higher time resolution, most of the events observed simply disappear into the noise; however, in a small number of cases, as low as 512 microsecond integration reveals certain bursts that do not disappear into the noise. I examined the cross-spectral output for all bursts remaining at the 512 microsecond integration level. In doing so, we have found a structure that we believe no one has seen before, particularly at this frequency band. These compact drifting bursts are created by some form of coherent emission with brightness temperatures on the order of 10^{11} K for the whole drifting group, or higher than 10^{13} K for a single peak within that group. On a different day, we see another burst that does not disappear at 512 microsecond integrations. These longer and less structured bursts have a brightness temperature on the order of 10^8 K.

After spending many hours trying to understand these drifting bursts, there are several different speculations that could explain what might be happening. The
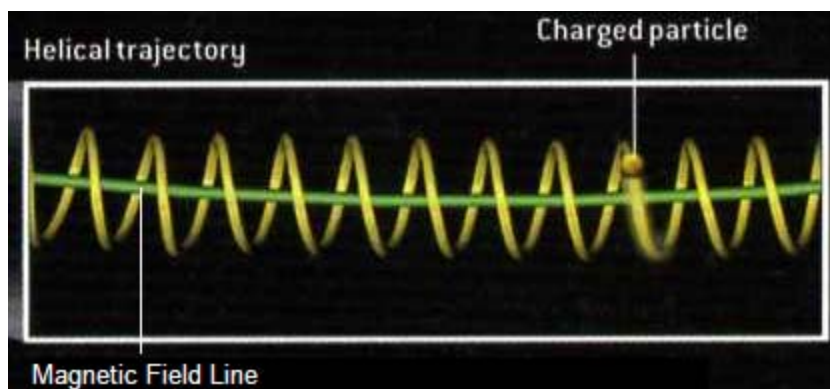

Figure 57 A charged particle following a helical path around a magnetic field line. If this particle is producing directed emission, it is plausible that we could see activity such as that observed on 13 Sep 2005 Image from *Scientific American* April 2006

general idea behind any of these speculations is that the emission occurs in an over-dense region of plasma in the corona. In this over-dense region, fundamental harmonic plasma radiation is produced. This radiation is not dissipated completely by free-free absorption because of the small size of this over dense region. The emission itself is most likely created in some way by moving electrons. Assuming that this emission mechanism is somewhat directed, then the emission must be traveling towards a less dense region of plasma following a helical path. It is very plausible for the electron path or the magnetic field to take on this helical pattern. We are still studying other efforts on the sun to better understand what we are seeing.

I have presented all phenomenological conclusions that we have to date. Work is moving forward with looking more in depth and soon to be observing more in an attempt to gather more drifting burst results.

There are still many questions to answer about every part of this study. First, if X-ray flares are caused by a single mechanism in varying strengths, as is the current theory, why would we only be guaranteed to observe a burst for flares above a certain
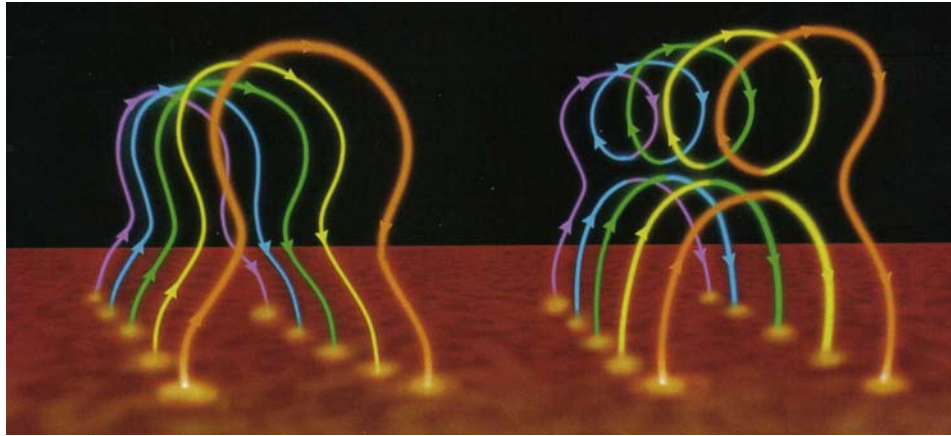

Figure 58 Before and After a magnetic reconnection event that creates a helical magnetic field. If an electron is moving along a path that follows a magnetic field line, it is possible to create emission that moves in a helical path in a situation like the picture above. Image from *Scientific American* April 2006

level? Is it possible that we were just lucky to only observe large solar flares that have a companion radio burst and that there exist some large flares without a radio companion? Is there a correlation between coronal mass ejections (CMEs) and radio bursts that determines if a radio burst is seen or not?

Moving on to the ground-breaking questions, what is the source of these frequency drifting bursts? Where does the very small scale structure come from? Why do these bursts drift at different rates? What causes some of these bursts to deviate from a linear frequency drift? What can cause variations on such short time scales and small frequency scales? Are the two types of short duration bursts observed created by the same mechanism? Is there some physical proximity to other solar activity that could help explain these events?

To answer some or all of these questions requires more in depth studies of the sun with extremely high time and frequency resolution. Additionally, dedicated instruments are needed so that the amount of time it takes to observe enough of these events to build an understanding is reasonable.

Acknowledgements

Bibliography

Aschwanden, M.J., Wiehl, H.J., Benz, A.O., & Kane, S.R. 1985, "Correlation of solar decimetric radio bursts with x-ray flares," *So.Ph.*, **97**, 159-172.

Bastian, T.S. 1991, "Solar radio microbursts at 1.4 GHz," *Ap.J.*, **370**, L49-L52.

Bastian, T.S., Benz, A.O., Gary, D.E., 1998, "Radio Emission from Solar Flares," *Annual Reviews Astro. Astrophys.*, **36**, 131-188.

Bastian, T.S, Gary, D.E. 1992, "Radio observations of the M8.1 Solar flare of 23 Jun, 1988: Evidence for energy transport by thermal processes," *So.Ph.*, **139**, 357-385.

Benz, A.O., et al. 2005, "Survey on solar x-ray flares and associated coherent radio emissions," *So.Ph.*, **226**, 121-142.

Benz, A.O., Kane, S.R. 1986, "Electron acceleration in flares inferred from radio and hard x-ray emissions," *So.Ph.*, **104**, 179-185.

Benz, A.O., Messmer, P. ,Monstein, C. 2001, "High-sensitivity observations of solar flare decimeter radiation," *A&A*, **366**, 326-330.

Bogod, V.M., Mercier, C., Yasnov, L.V. 2001, "About the nature of long-tern microflare energy release in solar active regions," *Journal of Geophysical Research*, **106**, A11, 25,353-25,360.

Bonnet, R.M. and Pauluhn, A. 2004, "Recent Progress and future prospects in solar physics, and their relevance for planet earth," *Surveys in Geophysics*, **25**, 371-440.

Dąbrowski, B.P. et al 2005, "Millisecond radio spike in the decimeter band and their related active solar phenomena", *A&A*, **434**, 1139-1153.

Dennis, B.R., 1988, "Solar flare hard x-ray observations," *So.Ph.*, **118**, 49-94.

Fárník, F., et al. 2002, "X-ray and radio observations in the initial development of an X-class solar flare," *Proc. SOHO 11 Symposium*, 441F.

Gopalswamy, N., Kundu, M.R. 1987, "Imaging observations of the evolution of meter-decameter burst emission during a major flare," *So.Ph.*, **111**, 347-363.

Harries, J.R., 1970, "Solar X-ray bursts and their relation to Hα and microwave emission," *So.Ph.*, **13**, 467-470.

Holman, G.D., 2006, "The Mysterious Origins of Solar Flares," *Scientific American*, April 2006, 39-45.

Kane, S.R., et al. 2003, "Hard x-ray and high-frequency decimetric radio observations of the 4 April 2002 solar flare," *Adv. Space Res.*, **32**, 12, 2503-2508.

Kraus, J.D. 1986, *Radio Astronomy*, 2nd ed.

Kundu, M.R. 1996, "Radio and X-ray imaging observations of solar flares and coronal transients," *So.Ph.*, **169**, 389-402.

Kuznetsov, A.A., Vlasov, V.G. 2003, "Solar millisecond spikes manifest large- and small-scale inhomogeneities of the coronal plasma," *Astronomy Reports*, **47,** 2, 129-138.

Lang, K.R. 2001, *The Cambridge Encyclopedia of the Sun*.

Lee, J et al. 2002, "Electron transport during the 1999 August 20 flare inferred from microwave and hard X-ray observations," *Ap.J.*, **572**, 609-625.

Livshits, M.A., Badalyan, O.G., Belov, A.V. 2002, "Common Features in the Development of Powerful Long-Duration Solar X-ray Flares," *Astronomy Reports,* **46,** 7, 597-608.

McConnell, D. 1982, "Spectral Characteristics of Solar S Bursts," *So.Ph.*, **78**, 253-269.

McConnell, D. 1983, "Evidence for Arc Sec Radio Burst Sources in the Upper Corona," *So.Ph.*, **84**, 361-369.

Meléndez, J.L., Sawant, H.S., Fernandes, F.C.R., & Benz, A.O. 1999, "Statistical Analysis of High-frequency decimetric type III bursts," *So.Ph.*, **187**, 77-88.

Rogers, A.E.E. 2005, *SRT Memos*, http://www.haystack.mit.edu/edu/undergrad/srt/SRT Memos/memoindex.html, #18, 19, 20.

Sawant, H.S., et al 1990, "Hard X-rays and Associated weak decimetric bursts," *So.Ph.,* **130**, 57-73.

Silva, A.V.R, Wang, H., Gary, D.E. 2000, "Correlation of microwave and hard x-ray spectral parameters," *Ap.J.*, **545**, 1116-1123.

Subramanian, K.R., Gopalswamy, N., Sastry, Ch.V., 1993, "A new investigation of microbursts at meter-decameter wavelengths," *So.Ph.*, **143**, 301-316.

Thompson, A.R., Moran, J.M., & Swenson, G.W. 1986, *Interferometry and Synthesis in Radio Astronomy*.

University of Sydney, 2003, "Brief History of Stellar Interferometry," http://www.physics.usyd.edu.au/astron/susi/susi_history.html.

Vilmer, N., 2003, "Hard X-ray and metric/decimetric spatially resolved observations of the 10 April 2002 solar flare," *Adv. Space Res.*, **32**, 12, 2509-2515.

Wikipedia, "Double-slit Experiment," http://en.wikipedia.org/wiki/Double-slit_experiment.

Yasnov, L.V, Bogod, V.M., Fu, Q., Yan, Y. 2003, "A study of non-thermal radio emission features using fine spectral bao and high-sensitivity rattan observations of a solar active region," *So.Ph.*, **215**, 343-355.

Appendix: Pertinent SRT Memos

MASSACHUSETTS INSTITUTE OF TECHNOLOGY
HAYSTACK OBSERVATORY
WESTFORD, MASSACHUSETTS 01886

June 13, 2005

To: SRT Group

From: Alan E.E. Rogers

Subject: Interferometer geometry calculations

For the "VLBI" mode we start with the latitude, longitude and height of each end of the "baseline" and convert to geocentric right handed *x, y, z* coordinates. This coordinate conversion is done by function

$$x = (n + hgt)\cos(lat)\cos(lon)$$
$$y = (n + hgt)\cos(lat)\sin(lon)$$
$$z = (n + (1-e) + hgt)\sin(lat)$$

where $n = a \big/ \left(1 - e\sin^2(lat)\right)^{\frac{1}{2}}$

        $a = 6378137$ m   WGS84
        e = 2f-f ^{2}
        f = 1/298.257223563 WGS84

The vector baseline is defined as the vector from site1 (the "reference" site) to site2 (the remote site)

$$b_x = x_2 - x_1$$
$$b_y = y_2 - y_1$$
$$b_z = z_2 - z_1$$

The delay τ of a signal's arrival at the remote site is $\tau = -\vec{b}\cdot\hat{s}/c = -\left(b_x s_x + b_y s_y + b_z s_z\right)/c$

Where c = velocity of propagation
        $\hat{s}$ = unit vector in the direction of the source
        s_x = cos (dec) cos (gha)
        s_y = -cos (dec) sin (gha)
        s_z = *sin(dec)*

where   *gha = gst – ra* = Greenwich hour angle
        gst = Greenwich sidereal time

> ra = apparent right ascension
>   dec = apparent declination

or from the derivatives of the phase with respect to r*a* and dec

$$\phi = (2\pi/\lambda)\big(\cos(dec)\cos(gha)b_x - \cos(dec)\sin(gha)b_y + \sin(dec)b_z\big)$$

In units of fringes per arc second

$$u = \big(b_x \sin(gha) + b_y \cos(gha)\big)\big(\pi/648,000\lambda\big)$$
$$v = \big(b_z \cos(dec) - b_x \cos(gha)\sin(dec) + b_y \sin(gha)\sin(dec)\big(\pi/648,000\lambda\big)\big)$$

The interferometer phase (normally defined as being positive (NRAO's convention) when the signal arrives earlier at the 2nd site is

$$\phi = +2\pi\vec{b}\cdot\hat{s}/\lambda \quad (radians)$$
or $\phi = -2\pi\tau f \quad (radians)$
where λ = wavelength (m)
        f = frequency (Hz)

The components of the baseline projected in the direction of the source in the directions of increasing RA and increasing declination are known as *u* and *v* and are often expressed in units of fringes per arc second. These can be derived from the baseline projections

$$u = b_x \sin(gha) + b_y \cos(gha)$$
$$v = b_z \cos(dec) - b_x \cos(gha)\sin(dec) + b_y \sin(gha)\sin(dec)$$

MASSACHUSETTS INSTITUTE OF TECHNOLOGY
HAYSTACK OBSERVATORY
WESTFORD, MASSACHUSETTS 01886

June 13, 2005

To: SRT Group

From: Alan E.E. Rogers

Subject: VLBI data correlation

A] Real correlation function

Memo 16 describes the format of the data files in the "VLBI" mode. The data is quantized as data files in the "VLBI" mode. The data is quantized as one bit per sample so that the "Van Vleck" correction [1] can be used to derive the continuous correlation function $R_{xy}(\tau)$ from the 1-bit or "clipped" correlation $\rho_{xy}(\tau)$ as follows:

$$R_{xy}(\tau) = \sin\left((\pi/2)\rho_{xy}(\tau)\right)$$

The clipped correlation function has been normalized by the number of bits correlated so that

$$\rho_{xy}(\tau) = (1/N)\sum_{t=0}^{t=N-1} x(t)\, y(t-\tau)$$

where 1 bit data from each antenna, *x(t)* and *y(t)*, take on values of +1 and -1.

The 1-bit clipped data is cross-correlated using a table look-up method. The function *xcorr( )* places the data into 32 bit words. The bits are correlated using the "exclusive OR" operation and a table look-up is done on each upper and lower 16 bits. The *xinit( )* function is used to get the correlation of each 16 bit block. The results are stored in the cc[ ] array for efficient access. The lag, τ, is changed by using the shift operations.

B] Cross-spectral function

The cross-correlation is covered to a cross-spectral function *s$_{xy}$(w)* given by

$$s_{xy}(w) = \sum_{\tau=-L/2+1}^{\tau=L/2} R_{xy}(\tau)\, e^{-i2\pi w\tau/M}$$

C] Complex correlation

The complex correlation (or delay function [2]) is derived using a reverse FFT transform

$$D(\tau) = \sum_0^{M-1} s_{xy}(w)e^{i2\pi w\tau/2M}$$

This sum can be obtained setting the negative frequencies to zero and doubling the FFT size to provide interpolation of the delay τ.

Since the sample rate is 8 Ms/s the spacing of the lags is 125 ns. The doubling of the number of points in the reverse FFT makes the spacing of the delay points 62.5 ns. The delay is determined by finding the maximum magnitude of the delay function and using parabolic interpolation between points so that

$$\tau = \tau_{max} + \left(P_{max+1} - P_{max-1}\right)^2 \Big/ \left(4P_{max} - 2P_{max+1} - 2P_{max-1}\right)$$

where $P = |D|^2$ and τ is in units of 62.5 ns. The interpolated maximum is

$$P = P\max + \left(P_{max+1} - P_{max-1}\right)^2 \Big/ \left(16P_{max} - 8P_{max+1} - 8P_{max-1}\right)$$
$$P = 2P^{1/2}/M$$

while the phase is $\mathrm{atan}2\left(Im D_{max}, \mathrm{Re}\, D_{max}\right)$

1] VanVleck, J.H. Middleton, D., *Proc IEEE*, **54**, 2, 1966.

2] Rogers, A.E.E., *in Methods of Experimental Physics*, **12**, part c, edited by M.L. Meeks, Academic Press, New York, 1976.

3] Thompson, A.R., Moran, J.M. and Swenson, G.W., *Interferometry and Synthesis in Radio Astronomy*, Wiley, New York, 2001.

MASSACHUSETTS INSTITUTE OF TECHNOLOGY
HAYSTACK OBSERVATORY
WESTFORD, MASSACHUSETTS 01886

July 5, 2005

Telephone: 978-692-4764
Fax: 781-981-0590

To: SRT Group

From: Alan E.E. Rogers

Subject: VLBI data signal analysis

This memo summarizes the signal analysis.

1] Geometry calculations

Each second the Apriori baseline delay and delay rate are calculated. The delay for each VLBI data block is calculated for each VLBI data block using the rate to interpolate the delay between seconds. Each block is 512 bytes (4096 samples) of 512 microseconds duration.

2] Data correlation

The data is correlated with an Apriori offset which is the nearest integral number of 125 nanoseconds sample: shift = (delay/125) where τ is in nanoseconds

$$\rho_{xy}(\tau) = (1/N) \sum_{t=0}^{t=N-1} x(t) y(t + shift - \tau)$$

The first 8 bytes of the data are excluded from the correlation because they contain block ID and total power information.

3] Clipping correlation

The quantized data correlation is converted to an estimate of the true correlation using the "VanVleck" clipping correction

$$R_{xy}(\tau) = \sin\left((\pi/2)\rho_{xy}(\tau)\right)$$

4] Cross-spectral function

The correlation function is transformed to the cross-spectral function

$$S'_{xy}(w) = S_{xy}(w)e^{-i(w\Gamma + \phi)}$$

where $w\Gamma = 2\pi kF/M$

1

M = size of FFT used to get cross-spectrum (256)

F = fractional delay in units of the sample period (known in VLBI as the "fractional bit")

ϕ = fringe rotation phase in radians

For the upper sideband system of the SRT

$$\phi = (2\pi) \times delay(\text{secs}) \times frequency(Hz)$$

6] Coherence averaging of the cross-spectrum

Following the "fractional bit" correction and fringe rotation the cross-spectrum can be averaged for a period up to the expected coherence time.

$$S_{av} = \sum_{0}^{M/2} S$$

We only need to average the positive frequencies, since the negative frequencies are redundant and are not used.

7] Estimation of the normalized correlation amplitude and residual delay and phase we now transform the cross-spectrum back to form a "delay function" using a larger FFT to avoid losses in the interpolation of the amplitude, delay and phase when the peak falls between output points. A doubling of the FFT size to 2M is adequate if parabolic interpolation is used between points.

The delay function is $D(\tau) = \sum_{0}^{M-1} S_{xy}(w) e^{i2\pi w\tau/(2M)}$.

The interpolated amplitude A, delay d and phase ϕ are

$$d = (k + F) \times 62.5 \quad ns$$
$$\phi = a\tan 2(\operatorname{Im} D_k, \operatorname{Re} D_k) - (\pi/4)F \quad radians$$
$$A = \left(\frac{2}{MN}\right)\left[p_k + (p_{k+1} - p_{k-1})F/4\right]^{1/2}$$

where $\quad F = (p_{k+1} - p_{k-1})/(4p_k - 2p_{k-1} - 2p_{k+1})$

$p_k = |D|^2$

k = index for which $|D|^2$ is a maximum

N = number of blocks in coherent integration period.

References:

1] VanVleck, J.H., Middleton, D., *Proc IEEE*, **54**, 2, 1966.
2] Rogers, A.E.E., *in Methods of Experimental Physics*, **12**, part c, edited by M.L. Meeks, Academic Press, New York, 1976.
3] Thompson, A.R., Moran, J.M. and Swenson, G.W., *Interferometry and Synthesis in Radio Astronomy*, Wiley, New York, 2001.